Nicholas Tyler Ogasa

Earth and Planetary Sciences

McGill University, Montreal

Constraining the fault-valve model

at Val-d'Or, Quebec

April 15, 2019

A thesis submitted to

McGill University

in partial fulfillment of the

requirements of the degree of

Master of Science Geology

Advised by

James D. Kirkpatrick

and coadvised by

Vincent J. van Hinsberg

TABLE OF CONTENTS

LIST OF FIGURES

Preface

Acknowledgements

Foremost, I would like to express my sincere gratitude to my advisor Prof. James D. Kirkpatrick for his support throughout this project, his expertise and passion for the field of structural geology, and his patience with me. His guidance benefitted this project in more ways than can be listed and much of what I have learned during the execution of this project I owe to him. Additionally, I would like to recognize the support I received from my coadvisor, Prof. Vincent J. van Hinsberg. His expertise in the fields of geochemistry and thermodynamics were essential to the goals of this project and I greatly appreciated his guidance and patience while working at McGill.

This work would not have been possible without the support of Eldorado Gold Co., which provided us with access to underground operations at the Triangle mine, knowledge of the local geology, and lodging during our fieldwork. I would also like to thank the Cité de l'Or Museum for allowing us open access to the Lamaque mining pit. Additionally, I would like to thank DIVEX and GEOTOP for their support in the form of scholarships.

I would like to acknowledge the contributions by Stan Roozen as a field assistant to this project. I greatly appreciated his support and company in the field and our discussions regarding thermodynamics and geochemistry, which greatly benefited this project. I would like to thank William Minarek and John Stix for being a part of my Thesis Committee and for providing feedback during annual committee meetings. Finally, I would like to thank Lang Shi for his expertise, guidance and assistance with the electron microprobe at McGill University.

Author Contributions

Chapter 1.

All writing was completed by Nicholas T. Ogasa, with editorial advice from James D. Kirkpatrick. Goals and objectives for the project were proposed by J.D. Kirkpatrick and Vincent J. van Hinsberg and discussed with N.T. Ogasa, J.D. Kirkpatrick, and V.J. van Hinsberg.

Chapter 2.

Field measurements and data were collected by N.T. Ogasa, J.D. Kirkpatrick, and Stan Roozen. Samples were collected by N.T. Ogasa and S. Roozen. Sample preparation was done by N.T. Ogasa. Tourmaline thermometry was performed by N.T. Ogasa, with assistance from V.J. van Hinsberg and S. Roozen. Compositional measurements were conducted by N.T. Ogasa with assistance from S. Roozen and Lang Shi. Pseudosection modelling was conducted by N.T. Ogasa and V.J. van Hinsberg. All calculations were conducted by N.T. Ogasa with assistance from J.D. Kirkpatrick and V.J. van Hinsberg. Tensile test experiments were designed by N.T. Ogasa and J.D. Kirkpatrick and were performed by N.T. Ogasa. All ideas presented were discussed between N.T. Ogasa, J.D. Kirkpatrick and V.J. van Hinsberg. All writing was completed by N.T. Ogasa, with editorial advice from J.D. Kirkpatrick and V.J. van Hinsberg.

Chapter 3.

All writing was completed by N.T. Ogasa, with editorial advice from J.D. Kirkpatrick. Ideas presented were discussed with J.D. Kirkpatrick.

Abstract

The fault-valve model is a conceptual model widely accepted to describe how overpressured fluids can promote seismic failure by lowering effective stresses. Faults and shear zones exposed at the Triangle and Lamaque mines at Val-d'Or, Quebec show evidence of mixed deformation and fault-valve behavior within a compressive setting. Quartz-tourmaline veins hosted within shear zones can be grouped into a subhorizontal set known as "flats" and a steeply dipping set known as "steeps." The orientations of these veins show an Andersonian paleostress field orientation with a horizontal σ_1 and vertical σ_3. The magnitudes of the fluid pressure cycling and stress cycling that occurred within the system are constrained and presented in this study. Tourmaline fibers within the veins are oriented parallel to the shear direction, and their tensile strengths were measured via tensile tests and the peak strength value (44 MPa) is used here as a proxy for the shear strength of the structures. This shear stress corresponds with differential stress values of 35 MPa for a fault dipping 56˚ and 105 MPa for a fault dipping 70˚. A deformation temperature of 308˚ C was determined via tourmaline intersector thermometry. The lithostatic pressure was estimated from geothermal and pressure gradients to be between 258 to 307 MPa. The liquid-vapor equilibrium pressure was calculated to be P_E = 9 to 10 MPa. The estimated minimum shear stress drop is 44 MPa and the estimated pressure drop is 222-267 MPa. Our results imply a very high pore fluid factor ($\lambda \approx 0.9$) would have been necessary for these structures.

Le modèle fault-valve est un modèle conceptuel largement accepté pour décrire comment les fluides en état de surpression peuvent produire une rupture sismique en réduisant les contraintes effectives. Les mines de Triangle et Lamaque à Val-d'Or, Québec, montrent des signes de déformation mixte et de comportement de fault-valve dans une configuration de compression. Les veines de quartz-tourmaline se situant dans les zones de cisaillement peuvent être regroupées dans un ensemble subhorizontal sous le nom de « plats » et un ensemble fortement incliné sous le nom de « raides ». Les orientations de ces veines montrent une orientation de champ de paléocontrainte d'Anderson avec un σ_1 horizontal et un $\sigma_3$vertical. Les magnitudes des cycles de pression de fluide et de contrainte qui ont lieu dans le système sont

contraintes et présentées dans cette étude. Les fibres de tourmalines situées dans les veines sont orientées parallèlement à la direction de cisaillement et leurs résistances à la traction ont été mesurées grâce à des tests de traction. La valeur maximale de résistance (44 MPa) est utilisée comme un indicateur de la valeur de résistance au cisaillement des structures. Cette contrainte de cisaillement correspond à une valeur de contrainte différentielle de 35 MPa pour une faille inclinée à 56° and de 105 MPa pour une faille inclinée à 70°. Une température de déformation a été évaluée à 308°C en utilisant la thermométrie intersectorielle de la tourmaline. La pression lithostatique a été estimée à partir de gradients géothermique et de pression entre 258 et 306 MPa. La pression d'équilibre liquide-vapeur a été calculé comme étant P_E = 9 à 10 MPa. La chute de contrainte cisaillante minimale estimée est de 44 MPa et la chute de pression estimée est de 222-267 MPa. Nos résultats impliquent qu'un facteur de fluide dans les pores très élevé ($\lambda \approx 0,9$) aurait été nécessaire pour ces structures.

Chapter 1 - Introduction

1.1 *Shear strength at the Brittle-ductile Transition Zone*

Faults and shear zones are common structures observed in the Earth's crust, and their formation and activity are controlled by a variety of mechanisms. Initially a two layer model for faults and shear zones in the crust was proposed, with elastic-frictional behavior producing brittle faults and fractures in the upper crust and crystal-plastic deformation mechanisms producing ductile shear zones in the lower crust (Sibson, 1977). This model predicted that shear resistance would reach a maximum value at the transitional boundary between these two layers. Scholz (1988) later recognized that this transition is not an abrupt boundary but rather a broad, semi-brittle zone where deformation is accommodated partly by frictional sliding and partly by bulk plastic deformation (see Fig. 1.1).

Within the shallow, brittle regime of the crust, rocks will respond to stress via fracturing, frictional sliding and cataclastic flow (Scholz, 1988). Fracturing occurs in response to an applied differential stress and may involve the reactivation of a preexisting fracture or the nucleation of a brand-new fracture where none was present before. Fractures can occur as either extensional (mode I) or shear fractures (mode II or III), or as hybrid fractures, which involve some combination of these two modes (Passchier and Trouw, 2005; Scholz, 1988).

The pore fluid pressure (P_f) in rocks is typically between the hydrostatic pressure (P_H) (the pressure of a column of water at a particular depth) and the lithostatic pressure (P_L) (the pressure of a column of rock at a particular depth) (Passchier and Trouw, 2005; Scholz, 1988; R. H. Sibson, 1990). P_f can be increased by pore volume reduction via deformation, metamorphic dewatering reactions, or loss of surface connectivity (Passchier and Trouw, 2005; Phillips and Powell, 2010). If $(\sigma_3 - P_f) \geq -T$ and $(\sigma_1 - \sigma_3) \leq 4T$ with T as the tensile strength of the rock, then an extension fracture will form (Boullier and Robert, 1992; Kerrich and Allison, 1978; Sibson et al., 1988). If the differential stress $(\sigma_1 - \sigma_3)$ is large enough, then slip will occur in the faults (R. H. Sibson, 1990).

Extension fractures open in the direction of the minimum principal stress component, which theoretically should be orthogonal to the direction of maximum compression (Anderson,

1905; Scholz, 1988). Extension fractures are dilational structures which given enough time, will fill with fluids that travel along pressure gradients through the surrounding rock (Passchier and Trouw, 2005; Scholz, 1988; Sibson et al., 1988). The presence of fluids within an extension fracture may result in mineralization and formation of a vein that can record the fluid composition and conditions (Robert and Brown, 1986a; Robert and Kelly, 1987). This mineralization may record multiple reopening events in the form of mineral bands, referred to as a "crack-seal texture" (Boullier and Robert, 1992; Robert and Brown, 1986b). Each mineralization event will produce at least a single mineral band, and subsequent reopening events will produce open space for subsequent bands to mineralize (Boullier and Robert, 1992; Passchier and Trouw, 2005; Robert and Brown, 1986b; Secor, 1965).

Shear fracturing involves some component of sliding by fracture surfaces, resulting in the displacement of markers on either side of the fracture. The most well-known shear fractures are faults. Slip within a shear fracture is largely governed by the laws of friction (Byerlee, 1978). Byerlee (1978) showed that for faults in the upper crust the shear stress necessary to cause sliding (τ), or frictional strength, increases with normal stress (σ_n) as described by equations 1.1 and 1.2 and noted that rock type has little to no effect on frictional strength. However, assuming a single frictional strength for an entire fault plane disregards diverse fault geometry and changes in lithology that can cause stress heterogeneities and is likely a great oversimplification.

$$\tau = 0.85\sigma_n \quad \text{for } \sigma_n \leq 2 \text{ kbar} \quad \text{(Eq. 1.1)}$$

$$\tau = 0.5 + 0.6\sigma_n \quad \text{for } \sigma_n > 2 \text{ kbar} \quad \text{(Eq. 1.2)}$$

A result of non-planar fault geometry are small misoriented segments of faults known as stepovers (Micklethwaite, 2013; Micklethwaite et al., 2014). These stepovers are not aligned with the shear direction of the fault, and will either result in local compression or dilation (Micklethwaite, 2013; Micklethwaite et al., 2014). During slip, dilational stepovers will increase permeability and have been associated with gold mineralization and enhanced fluid flow (Micklethwaite, 2013).

Cataclasis involves the crushing or milling of rock, typically during fault slip, resulting in a reduction in grain size, which can reduce permeability and promote cementation (Scholz, 1988). Cataclastic flow involves the accommodation of slip by rotation of grains produced via cataclasis (Scholz, 1988). It is important to note that cataclastic flow may appear ductile at the macroscopic scale, but can be identified as a brittle mechanism due to its strong pressure dependence and the significant dilatancy that is involved (Scholz, 1988). Any cataclastic flow would most likely occur near the shallowest parts of the brittle-ductile transition zone (BDTZ) (Scholz, 1988).

In the lower crust, higher temperatures favor crystal plastic deformation over brittle mechanisms (Sibson 1977). At these depths, the thermally activated migration of mineral lattice

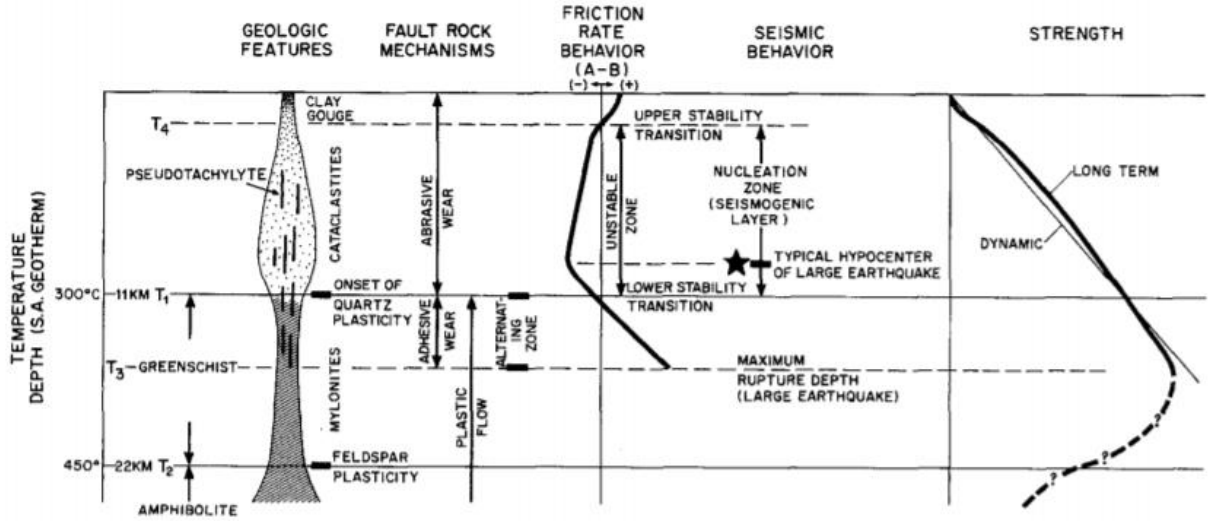

Figure 1.1 An illustrated model of a shear zone, with various characteristics included. The "alternating zone" in this figure represents the brittle-ductile transition zone. Taken from Scholz (1988).

defects allows for the plastic flow of rocks under stress, resulting in the formation of shear zones (Burgmann and Dresen 2008). Shear zones are geologic structures which accommodate slip across a non-discrete zone with increasing degrees of strain towards the center (Bürgmann and Dresen, 2008; Döhmann et al., 2019; Scholz, 1988). It is at the centers of shear zones where highly stretched and flattened foliated rocks like mylonites are most often found (Döhmann et al., 2019). The localization of strain into shear zones is a consequence of rheological heterogeneities in rock (Döhmann et al., 2019). Many shear zones act as channels for lower

crustal fluids, and the presence of these fluids will weaken the strength of the shear zone—this is known as hydrolytic weakening (Bürgmann and Dresen, 2008). Flow laws based on laboratory experiments have been used to estimate shear zone strength in the plastic regime (Burgmann and Dresen 2008), but these formulas are typically representative of single minerals and require extrapolation to geologic strain rates and temperatures.

The BDTZ is a field of mixed deformation, within which crystal-plastic processes begin to thermally activate due with increasing depth and temperature (Scholz 1988). For quartzo-feldspathic rocks, crystal-plastic mechanism will begin to activate at temperatures between 300-450˚ C (Scholz, 1988). For reference, greenschist facies metamorphism in the same rock type will typically take place around 300˚ C. Between 300-450˚ C, it would expected that quartz would flow in a crystal-plastic manner around feldspar, which would fracture and form porphyroclasts (Scholz, 1988). The thickness of the BDTZ will increase in less homogenous rocks, due to the varying ductility of different components (Scholz 1988). It therefore represents a gradational boundary between the two deformation regimes, where brittle and plastic processes require similar applied stresses to accommodate deformation and compete for dominance (Scholz 1988). Due to the onset of crystal-plastic flow, strength estimates obtained via frictional experiments are not applicable at this depth (Scholz, 1988). Likewise, flow laws used to estimate strength in the ductile regime cannot be extrapolated into the BDTZ, since flow in the BDTZ is sensitive to pressure, so flow laws will always underestimate the strength of the BDTZ (Scholz, 1988). Descending through the geothermal gradient, high enough temperatures are reached so that frictional surfaces will weld together and prevent rupture nucleation, although large earthquakes may propagate to greater depths (Scholz, 1988). This depth, below which earthquake nucleation ceases, is referred to as the base of the seismogenic zone and is typically where the largest earthquakes occur (Scholz, 1988; Sibson et al., 1988). Not surprisingly, the base of the seismogenic zone is considered to be the strongest depth in the earth's crust (Scholz, 1988). Despite this, direct and indirect measurements of the strength of rocks at this depth are lacking.

1.2 *Orogenic Gold*

Orogenic gold deposits are located around the world and have produced a significant portion of the world's gold supply (Goldfarb et al., 2001). These deposits form a broad and diverse category which are principally united by an association with metamorphic terranes and major transcrustal structures (Goldfarb et al., 2001). Orebodies of this class form during deformation at collisional or accretionary plate margins, and are typically found within second to third-order structures located near large, transcrustal faults or shear zones, which are referred to as first-order structures (Groves et al., 1998). There is a general consensus that auriferous fluids are released during metamorphic devolatization at the greenschist-amphibolite facies transition and utilize the major transcrustal structures to migrate upwards into the smaller subsidiary structures (Goldfarb and Groves, 2015). This process typically produces quartz-dominant vein systems located within greenschist facies host rocks (Groves et al., 1998), and many of these orogenic vein systems include high-angle reverse or reverse-oblique shear zones that developed within regimes of horizontal compression or transpression (Boullier and Robert, 1992; Sibson et al., 1988). These veins are believed to be the product of intermittent fault slip associated with overpressured fluids and permeability fluctuations (Boullier and Robert, 1992; Sibson et al., 1988). Orogenic gold deposits have been suggested to have formed near the base of the seismogenic zone, due to the mixed deformation characteristically observed within them and greenschist facies mineral assemblages (Sibson et al., 1988).

1.3 *Geologic Setting of Val-d'Or, Quebec*

Figure 1.2 Map of eastern Canada, with the Abitibi Greenstone Belt highlighted in red. Taken from Monecke et al. (2017).

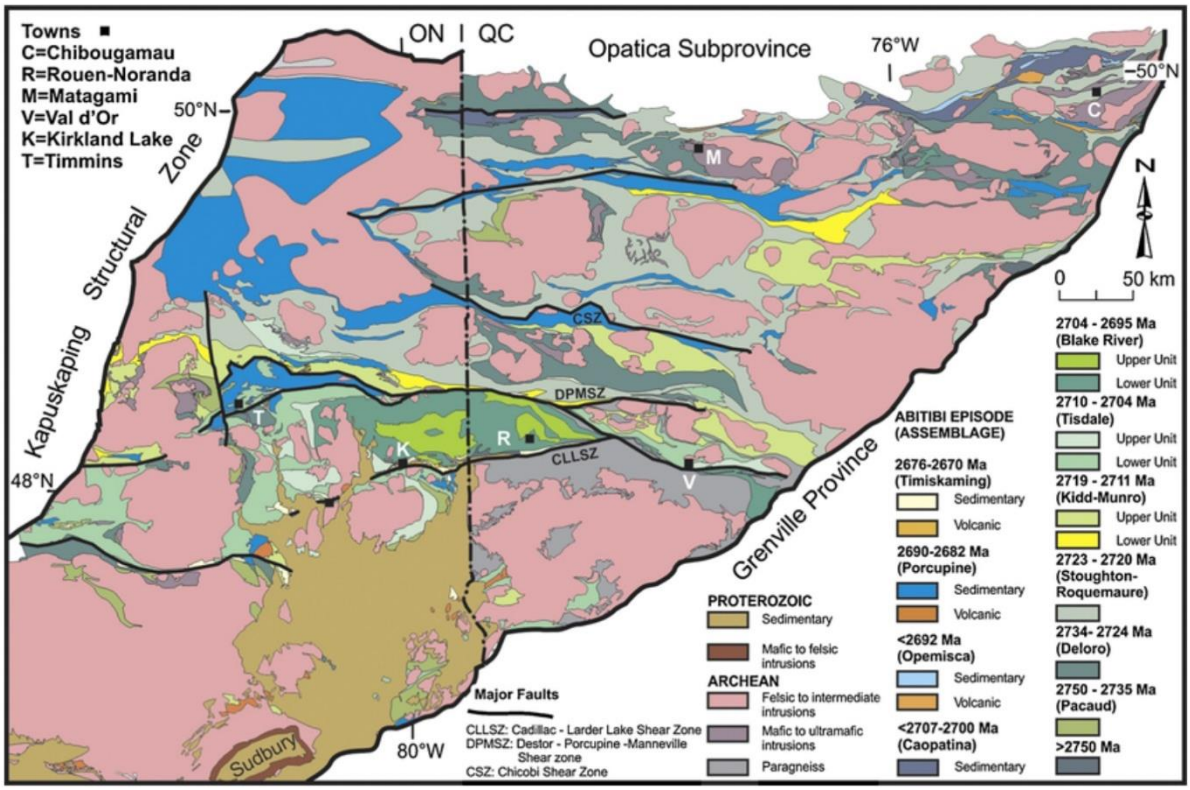

Figure 1.3 Geologic map of the Abitibi Greenstone Belt. The Cadillac Tectonic Zone (CTZ) is denoted by "CLLSZ". Taken from Bedard et al. (2013).

The Val-d'Or gold mining camp is located in northwestern Quebec, within the Abitibi Greenstone Belt (AGB), a massive greenstone terrane (Fig. 1.2, 1.3). The primary rock type in the AGB is a volcano-sedimentary assemblage, of which the volcanic rocks have been dated via K/AR dating to a minimum age of 2700 Ma (Robert and Brown, 1986b). These volcanic rocks are part of the Malartic Group, and near Val-d'Or consist mostly of felsic-mafic lava flows and pyroclastic rocks (Robert and Brown, 1986b). The Lower Malartic consists of mafic-ultramafic flows while the Upper Malartic consists of felsic-mafic flows with pyroclastic rocks (Robert and Brown, 1986b). Large felsic masses like the Bourlemaque batholith have intruded into the volcanics. The volcanic rocks have an E-W trending, vertical, tectonic regional foliation and have undergone greenschist facies metamorphism (Robert and Brown, 1986b).

Approximately 6 km south of Val-d'Or, the E-W trending Cadillac Tectonic Zone (CTZ) separates the AGB from the metasediments of the Pontiac Subprovince. While it has been

suggested that the CTZ may have initiated as part of a normal or wrench fault system (Dimroth et al. 1983; Hubert et al. 1984), the most recent movement has been shown to be reverse (Sibson et al. 1988). The CTZ constitutes a major first order structure to which the ore-bearing structures at Val-d'Or may be subsidiary (Sibson et al. 1988).

Multiple gold mines exist within the Val-d'Or district including the well-studied Sigma mine (Robert and Brown 1986a, 1986b; Sibson et al. 1988), the Lamaque mine, and the recently discovered Triangle mine (Fig. 1.4). These ore deposits in Val-d'Or are characteristic of the orogenic gold type deposit (Robert and Brown 1986a, 1986b; Sibson et al. 1988; Boullier and Robert 1992). Of these three mines, the Sigma mine is the oldest and largest, the most well studied, and has been in operation since 1937 (Robert and Brown, 1986b). The Triangle mine is the newest mine of the three, and unlike Sigma or Lamaque, Triangle is entirely an underground operation.

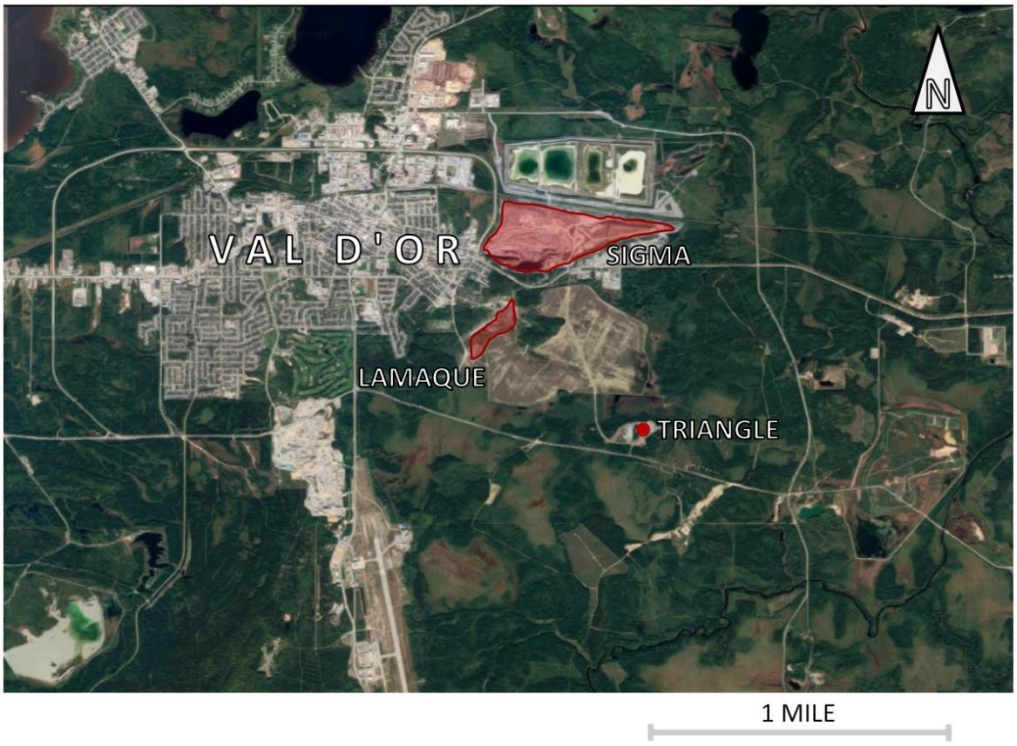

Figure 1.4 Map of Val-d'Or with mine locations shown in red. Lamaque and Sigma's open pit areas are highlighted and the entrance to the underground Triangle mine is marked.

The Sigma deposit is an auriferous quartz-tourmaline-carbonate vein network hosted within steeply dipping, E-W trending shear zones (Boullier and Robert, 1992; Robert and Brown, 1986b; Sibson et al., 1988). These shear zones dip approximately 70˚ to the south, and occur within the Upper Malartic Subgroup, which is composed of andesites with small lenses of pyroclastic rocks intruded by masses of porphyritic diorite and feldspar porphyry dikes (Robert and Brown, 1986b). The andesite contains flow contacts that dip approximately 090/80˚ N (Robert and Brown, 1986b). The porphyritic diorite-metavolcanics contact is crenulated by the E-W regional foliation, indicating that it was emplaced before that deformation event (Robert and Brown, 1986b). The feldspar-porphyry dykes crosscut the metavolcanics and porphyritic diorite, and dip approximately 80˚ to the north (Robert and Brown, 1986b). The dykes are not deformed, indicating they were emplaced after the regional foliation had formed (Robert and Brown, 1986b). All three rock types have undergone greenschist facies metamorphism, and contain plagioclase, quartz, chlorite, epidote, clinozoisite, which mica or biotite and minor ilmenite, apatite, pyrite and carbonates (Robert and Brown, 1986b). Within the dykes, the plagioclase is albitic, while in the volcanics and porphyritic diorite the plagioclase is more calcic in composition (Robert and Brown, 1986b).

Two sets of veins are recognized at Sigma—a steeply dipping set of shear veins that parallel the shear zones in orientation, and a subhorizontal set of “flats” exist (Fig. 1.5) (Boullier and Robert, 1992; Robert and Brown, 1986b; Sibson et al., 1988). Shear veins and flats are observed as both continuous and mutually crosscutting structures throughout the deposits, implying a degree of contemporaneity between the sets (Robert and Brown, 1986a; Sibson et al., 1988). Flats have been interpreted to be mineralized hydraulic extension fractures oriented perpendicular to the least compressive stress (σ_3 is interpreted to be vertical) that were held open by elevated fluid pressures (Robert and Brown, 1986b). The flats extend laterally from shear veins and mineral banding within flats records episodic opening and sealing (Robert and Brown, 1986b). Robert and Brown (1986b) show that the flats and shear veins share similar mineralogies, with an average vein composition of 80% quartz, 15% tourmaline, and minor

amounts of calcite, chlorite, sulfides, scheelite and other minerals. They also observe that at depths greater than 1300m below the surface, biotite is found in place of tourmaline in the veins. Recrystallization observed in vein quartz, brittle microfracturing in the tourmaline, and dragfolding of some flats indicate that the vein system at Sigma was structurally active at the depth of the brittle-ductile transition zone (Robert and Brown 1986a; Sibson et al. 1988; Boullier and Robert 1992). Fracturing and frictional slip would have been necessary to open space for veins to grow, and recrystallization within the veins indicates that deformation temperatures were high enough to thermally activate crystal-plastic mechanisms. As shown in Figure 1, the brittle-ductile transition zone lies at a depth similar to that of the greenschist-amphibolite transition, which is believed to be the primary source of the mineralizing hydrothermal fluids (Scholz 1988, Goldfarb and Groves 2015). Reverse motion in the shear veins, flat orientations, and conjugate reverse shear zones all indicate a vertical σ_3 and horizontal σ_1 (Fig. 1.5) (Sibson et al., 1988). Vein mineralization temperatures at Sigma have been estimated via analyses of fluid inclusions in quartz to 300-400˚ C (Robert and Kelly, 1987).

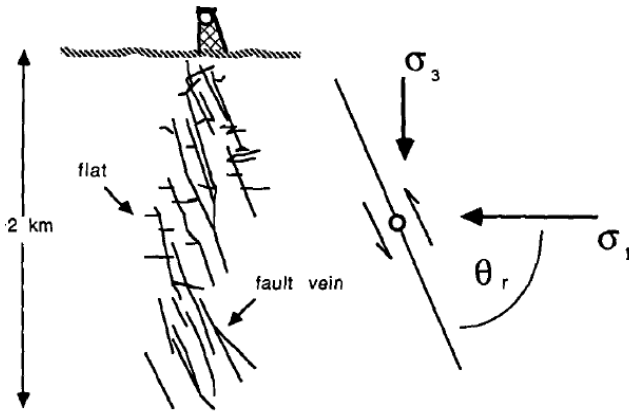

Figure 1.5 A schematic of the Sigma deposit vein system. A "fault vein" in this figure is synonymous with a "shear vein" or a "steep." Taken from Sibson et al. (1988).

All veins at Sigma are accompanied by envelopes of hydrothermally altered wall rock (Robert and Brown, 1986a). These alteration envelopes consist of three zones which are an outermost, invisible to the eye, chlorite-carbonate-white mica zone, an inner carbonate-white mica zone, and an innermost carbonate-albite zone (Robert and Brown, 1986a). These zones are the product of advancing reaction fronts with the innermost carbonate-albite zone having

the most intense alteration, and the outermost chlorite-carbonate-white mica zone having the least intense but most common alteration (Robert and Brown, 1986a). Oxygen isotope analyses of wall-rock alteration at Sigma give temperatures of 270-450˚ C (Kerrich, 1986).

The Lamaque mine is located approximately 1 km southwest of Sigma (Fig. 1.4) and is a quartz-tourmaline-carbonate vein system that occurs within shear zones in the Upper Malartic Subgroup. While andesitic flows and flow breccias exist at Lamaque, the chief volcanic rocks (approximately 60%) are pyroclastics (Perrault et al., 1984). These andesites and pyroclastics are intruded by (in order of decreasing age) a large mass of porphyritic diorite, porphyritic quartz-feldspar masses, and 100-200 m diameter diorite and tonalite plutons (Fig. 1.6) (Perrault et al., 1984). All rock types have undergone greenschist facies metamorphism (Perrault et al., 1984). As is found at Sigma, all veins are accompanied by envelopes of hydrothermal alteration with an outer invisible zone that is always present, and inner zones that can be observed in the field and reflect higher degrees of alteration (Perrault et al., 1984).

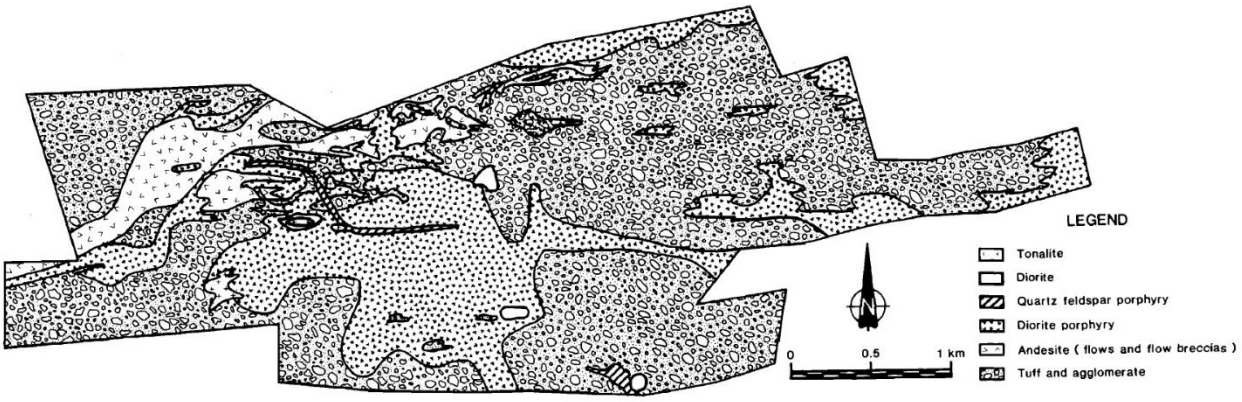

Figure 1.6 Map view of the geology present at the Lamaque mine. Taken from Perrault et al. (1984).

The Triangle mine is located approximately 3 km southeast of Sigma (Fig. 1.4), and like Sigma and Lamaque is a shear zone associated, quartz-tourmaline-carbonate vein system that is hosted in metavolcanics (Dubé, 2018). At the time of this study, the Triangle mine is an underground operation that has reached a depth of approximately 300 m. The dominant volcanic rocks at Triangle are a tuff unit comprised of lapilli tuff, lapilli and block tuff, block tuff,

and locally some crystal tuff (Dubé, 2018). Like the volcanics at Sigma and Lamaque, the Triangle tuff contains a regional foliation which indicates it formed prior to that deformation event (Dubé, 2018). The volcanic rocks are intruded by masses of porphyritic diorite and feldspar porphyry dykes (Dubé, 2018).

1.4 *The fault-valve model*

The fault-valve model as initially proposed by Sibson et al. (1988) calls upon elevated fluid pressures to lower the effective stresses necessary to cause slip. This mechanism that has been used to explain slip along faults oriented unfavorably in the prevailing stress field (Sibson et al., 1988). Within a compressive stress regime, faults favorably oriented for thrust reactivation should have dips that of approximately 22-32˚, assuming normal values for the coefficient of internal friction and an Andersonian stress field in which the least compressive principal stress is vertical (Byerlee, 1978). The Sigma mine at Val-d'Or is the type-locality for this mechanism, as Sibson et al. (1988) found structures there to be well exposed and to be representative of typical vein systems in the Val-d'Or district. Dips of the steeply dipping shear veins deviate from the optimal reactivation angle by greater than 15˚ and are indicative of fault-valve behavior.

The fault-valve model considers a sealed, fault/shear zone system in a compressive stress regime, where $\sigma_1 > \sigma_2 > \sigma_3$ and where the plane containing σ_1 and σ_3 is vertical (Sibson et al. 1988). Devolatilized fluids rising from the greenschist-amphibolite metamorphic transition travel along pressure gradients into the shear zone (Boullier and Robert 1992). As fluids infiltrate into and migrate up the shear zone they eventually encounter the impermeable base of the seismogenic zone, which effectively stops them from rising further (Sibson 1990a). The low permeability at this depth is likely due to solution transfer and sealing of fractures via mineralization at temperatures between 150 - 300˚ C (Sibson, 2014). As fluids accumulate at this barrier the pore fluid pressure will increase until pressures reach or exceed that of the lithostatic pressure and failure occurs (Sibson et al., 1988). If the differential stress is high enough then slip will occur within the reverse faults, but if not then extensional fractures will open instead. Boullier and Robert (1992) observed crushed mineral textures within flats at Val-

d'Or and interpreted these textures as records of intermittent stress reversals. They propose that the immediate loss in fluid pressure during slip resulted in a stress reversal and sudden vertical compression in the flats (Boullier and Robert, 1992). The phases of the fault-valve model are presented here.

Prefailure:

Fluids from beneath the impermeable seismogenic zone would accumulate and pressures would approach the magnitude of the lithostatic load (Sibson et al., 1988). These fluids are sourced from devolatization reactions at the greenschist-amphibolite metamorphic facies transition (Cameron and Hattori, 1987; Goldfarb and Groves, 2015). Any local magmatism would provide an additional source of fluids and of heat energy that drives convection of pre fluids, which would contribute to an increase in fluid pressure (Sibson et al., 1988).

Failure/Rupture:

When the fluid pressures finally reach or exceed the lithostatic load, extensional fracturing and/or fault slip will occur (Sibson et al. 1988). Reactivation of the faults will only occur if differential stresses are high enough, otherwise only subhorizontal extensional fractures will open (Boullier and Robert, 1992; R. H. Sibson, 1990). Extensional fractures will nucleate at a fault and propagate laterally outwards, in an orientation subperpendicular to σ_3 (R. H. Sibson, 1990). In the case of fault slip, an earthquake will propagate up fault towards the surface, producing fracture permeability and promoting fluid infiltration (Sibson et al. 1988). Immediately, shear stress and fluid pressures drop while permeability increases (Sibson et al. 1988). Boullier and Robert (1992) propose a total release of shear stress at this moment, accompanied by a transient reversal of the stress axes, indicated by normal deformation of calcite veins in the shear zones. Immediately following rupture, it is believed that the hydrothermal fluid undergoes a phase separation due to the sudden pressure drop (Robert and Kelly 1987). An exsolved gas phase is the first to infiltrate the newly formed open spaces in the faults, resulting in the precipitation of gold and other minerals (Fig 6) (Sibson et al. 1988, Boullier and Robert 1992).

Postfailure:

Fluids will flow into the open spaces and where they are able to interact with freshly exposed wall rock, hydrothermal alteration envelopes develop (Robert and Brown 1986b). These are zones of local metamorphism with assemblages that reflect the temperature, pressure, and chemical environment at the wall rock-fluid interface (Robert and Brown, 1986b). So long as the fault remains unsealed and fluids continue to flow into the fault, P_f likely remains near hydrostatic levels (Robert and Kelly 1987; Sibson et al. 1988).

Sealing period:

As fluids circulate through the permeable fracture network mineralization will occur, progressively lowering and eventually destroying permeability in the system (Sibson et al. 1988). Mineral growth will nucleate along fracture edges and grow inwards towards the center, resulting in the open-growth textures common to veins (Robert and Brown, 1986a, 1986b). Once faults and fractures have been fully mineralized, fluid pressure and shear stress will begin to rebuild below (Sibson et al. 1988).

The stresses and fluid pressures proposed by Sibson et al. (1988) in this model are unknown and instead a coefficient of friction $\mu = 0.75$ is typically assumed, representative of Byerlee values. Since then, knowledge of the strength of the crust at depth has improved and suggests that this value is not accurate (Scholz 1988). Additionally, no tests independent of frictional measurements have been done to establish the magnitudes of the effective stresses, particularly in the BDTZ. It is therefore of interest to constrain stresses and fluid pressures using methods independent of frictional measurements.

1.5 *Tourmaline as a geothermometer*

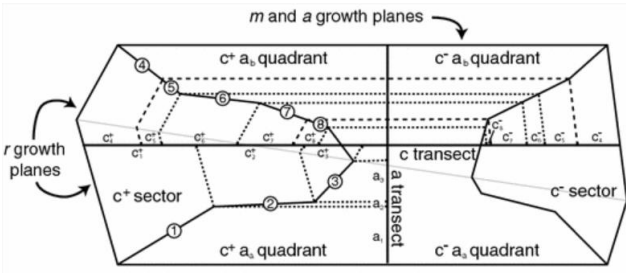

Figure 1.7 Schematic showing the sectors in a tourmaline crystal. The greatest compositional difference will occur between the c+ and c- sectors, while the a sector represents an intermediate, neutral composition. Taken from Hinsberg and Schumacher (2007).

Henry and Dutrow (1992, 1996) first proposed using partitioning between polar overgrowths in tourmaline as a thermometer. As a tourmaline crystal grows, the c- side of the crystal will attract more highly charged cations and develop a full X-site, whereas the c+ side of the crystal will attract lower charged cations and vacancies on the X-site (Henry and Dutrow 1992, 1996; van Hinsberg et al., 2006). Partitioning of Ca and Ti between the polar overgrowths is most significant, and this partitioning has been shown to be temperature-dependent (Henry and Dutrow 1992, 1996; Sperlich 1990). Henry et al. (1999) and van Hinsberg et al. (2006) expanded upon this thermometer by further subdividing the crystal into a number of sectors with different surface angles and site morphologies, which result in varying degrees of partitioning (Fig. 1.7). Similar to polar overgrowth compositional differences, intersector compositional differences have been shown to be temperature dependent and able to record temperature ranges of 300-650° C, and so tourmaline crystals provide a useful geothermometer (van Hinsberg et al. 2004, 2006, 2007).

Tourmaline occurs in the deposits at Val-d'Or within veins as bands or ribbons which represent distinct hydrofracturing events. We will analyze tourmaline crystals from different bands and determine the temperatures of the fluids during different events, which will assist in constraining the pressure drops associated with those events. This method will allow us to

measure temperatures during the mineralization of different tourmaline generations and may give us insight into the thermal evolution of the hydrothermal fluids and vein system. Where tourmaline has crystalized directly on fracture walls, we will be able to determine the exact temperatures during fracturing.

1.6 *Research Statement*

The goals of this project are to 1) study the exposed structures at Triangle and Lamaque to ensure consistency with the structural framework proposed at Sigma, and 2) place quantitative constrains (deformation temperature, paleostress magnitude, fluid pressure drop magnitude) on the fault-valve model at Val-d'Or, Quebec. In order to accomplish these tasks, we will utilize a variety of methods and analyses. To develop a relative timing and structural framework model for Triangle and Lamaque, we will collect structural measurements, sample the veins, wall rock and hydrothermal alteration, construct 3D models of outcrops, and record rock descriptions. Rock samples will be studied under a scanning electron microscope (SEM), a transmitted light microscope to determine their mineralogy, microstructures, and growth textures. In order to constrain the temperature of deformation, we use microstructural analysis and tourmaline intersector thermometry. The lithostatic pressure will be estimated using rock densities, our estimated deformation temperature, and a geothermal gradient. The fluid-vapor equilibrium pressure will be constrained by using a fluid equation of state. The strength of the faults at Val-d'Or are determined by performing tensile tests on tourmaline crystals. This manuscript is in preparation to be submitted to the Journal of Structural Geology.

Chapter 2 – Constraining the fault-valve model at Val-d'Or, Quebec

2.1 *Introduction*

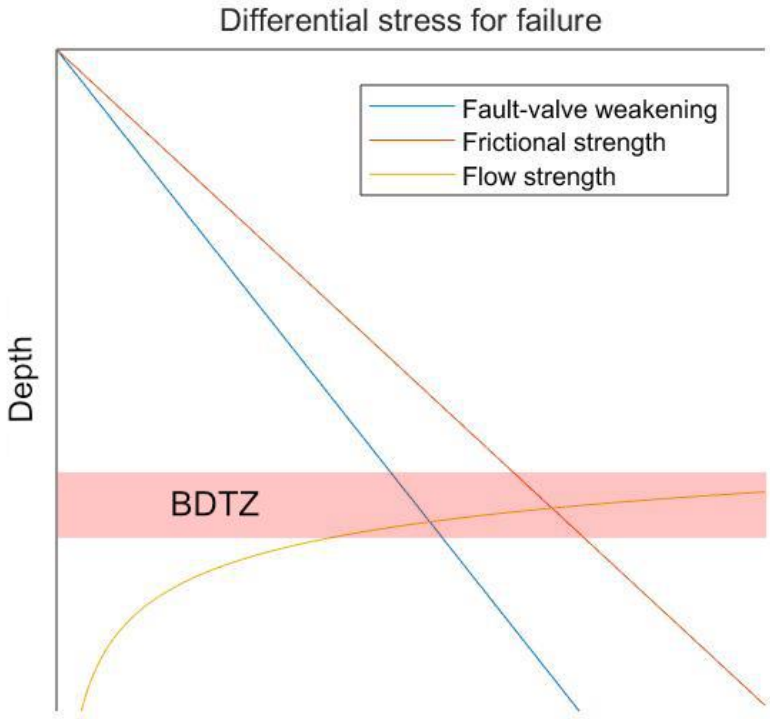

Figure 2.1 Crustal strength diagram showing frictional strength and flow strength, as well as fault-valve weakening of frictional strength.

From a geologic perspective, the earth's crust is a highly dynamic system in which tectonic forces may produce earthquake generating faults and slowly creeping shear zones. Faults and shear zones are common structures throughout the Earth's crust and constraining the strength of these structures is critical to our understanding of stress and strain in the crust. Sibson (1977) first proposed a two layer model for deformation in the crust, with elastic-frictional behavior producing faults and fractures in the brittle, upper crust and crystal-plastic deformation mechanisms producing shear zones in the ductile, lower crust (Sibson, 1977). Fault

strength is generally determined by frictional resistance, which is pressure-dependent and follows Mohr-Coulomb behavior. Within the ductile regime the strength of shear zones is extrapolated from steady-state flow laws and decreases exponentially with depth as crystal-plastic mechanisms are thermally activated (Scholz, 1988).

Since Sibson first proposed the two-layer model, it been recognized that the shift from brittle to crystal-plastic deformation mechanisms is not an abrupt horizon but rather a broad zone where deformation is accommodated partly by frictional sliding and partly by bulk plastic deformation (Fig. 2.1) (Scholz, 1988). This is known as the brittle-ductile transition zone (BDTZ), where temperatures are high enough for mineral lattice defects to migrate under differential stresses comparable to the frictional strength (Bürgmann and Dresen, 2008). Descending through the BDTZ, the primary form of deformation gradually shifts from frictional sliding and cataclastic mechanisms to crystal-plastic deformation mechanisms, and ultimately high enough temperatures are reached to weld surfaces together and frictional sliding ceases (Scholz, 1988). Earthquake nucleation is limited to the frictionally unstable portion of the brittle regime, known as the seismogenic zone, which overlies the BDTZ, however ruptures may propagate downwards below this seismogenic zone (Scholz, 1988). To reconcile the frictional and plastic behaviors, crustal strength profiles typically extrapolate friction measurements and flow laws to show that the greatest shear resistance occurs in the BDTZ at the depth where this welding occurs (Scholz, 1988; Stesky, 1978). Unfortunately, strength measurements derived from primary data collected from rocks that formed at this depth are lacking.

Orogenic gold deposits present an excellent opportunity to study the BDTZ, as many are believed to have formed near or at the brittle-ductile transition (Sibson et al., 1988). These deposits typically consist of quartz vein systems located in greenschist facies host rocks (Groves et al. 1998), and many are associated with high-angle reverse or reverse-oblique shear zones (Sibson et al. 1988). Orebodies of this class form during deformation at collisional or accretionary plate margins and are typically found within second to third-order structures located near large, transcrustal faults or shear zones (Groves et al. 1998; (Sibson et al., 1988). These structures are believed to have been exhumed from near the base of the seismogenic

zone due to their association with greenschist facies host rocks and mutually cross-cutting brittle and ductile structures (Sibson et al., 1988).

The Sigma deposit at Val-d'Or, Quebec is a characteristic orogenic gold deposit consisting of quartz veins hosted in high angle reverse faults (Boullier and Robert, 1992; Robert and Brown, 1986b; Sibson et al., 1988). Sigma is also the type locality of the fault-valve mechanism (Sibson et al., 1988). This conceptual model describes the process in which crustal fluids accumulate beneath the base of the seismogenic zone, eventually building up sufficient pore pressure to destabilize a fault and promote fault slip (Sibson et al., 1988). Postrupture, the overpressured fluids travel through newly opened space, mineralizing and ultimately sealing the fault (Sibson et al., 1988). The process will repeat once the fault is fully sealed and permeability is reduced (Sibson et al., 1988). Fault-valve behavior has large potential consequences for crustal strength, as at a depth of 10 km a change in the pore fluid factor (P_f/σ_3) of 0.05 may result in a strength increase of 10 MPa (Sibson, 1992). It is therefore of great interest to understand how significantly the fault-valve mechanism affects the strength of the crust at this depth.

This study focuses on the exposed faults and shear zones in the Sigma and associated Lamaque and Triangle deposits at Val-d'Or and treats these structures as records of the mixed deformation characteristic of the BDTZ. The faults contain slickensides with tourmaline fibers aligned subparallel to the shear direction inferred from slickenlines on the slip surfaces. These fibers were stretched and failed in tension during fault slip. Consequentially the tensile strength of tourmaline can be used a proxy for fault strength. Here, I present results from tests of tourmaline tensile strength performed at ambient room temperature (~16˚ C) and pressure. This technique provides an alternative method by which to estimate fault strength that does not rely on frictional measurements or flow laws and confirms that pore fluid pressures must have been near-lithostatic during faulting. An estimation of the pressure drop (the magnitude by which overpressured fluids reduce the effective stress) is additionally presented to assess the relative importance of stress and pore fluid pressure changes during fault valve faulting.

2.2 *Geologic Setting*

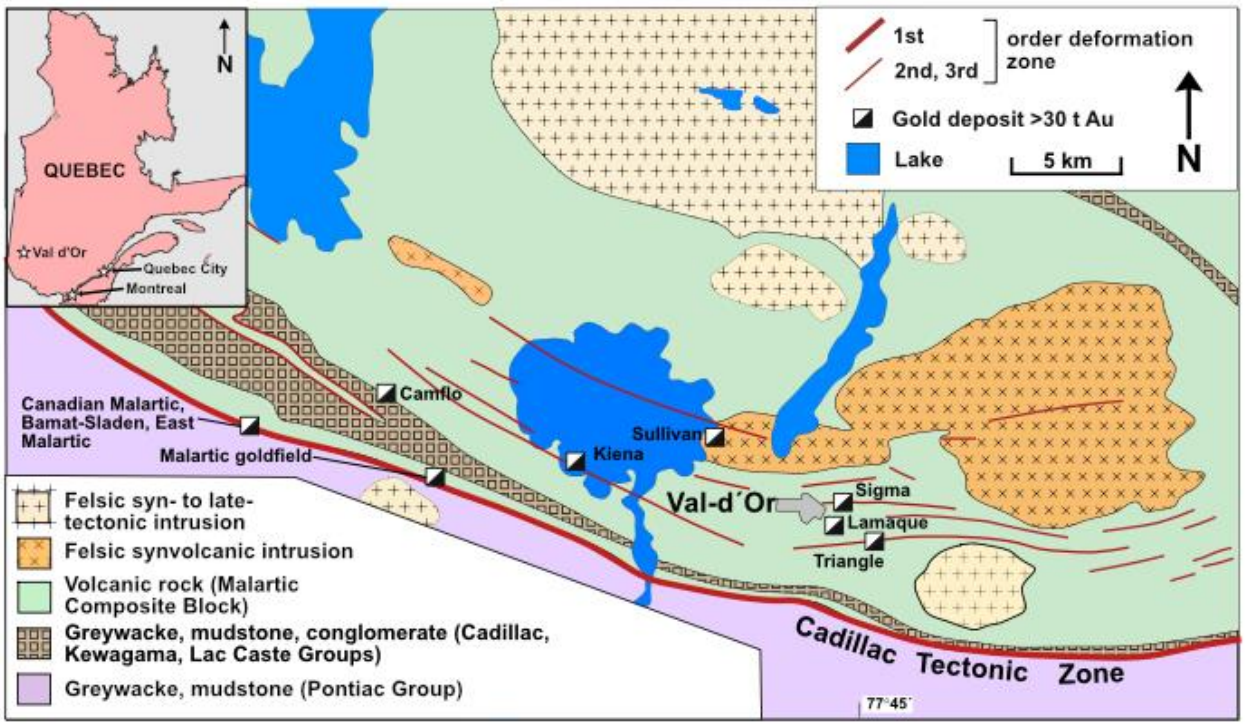

Figure 2.2 Simplified geologic map of the region surrounding Val d'Or. Modified from (Neumayr et al., 2007)

The Val-d'Or mining camp is located in northwest Quebec, in the southern Abitibi subprovince (SAS) (Fig. 2.2). Near Val-d'Or, the SAS is a metavolcanic-plutonic terrane chiefly comprised of greenschist-facies metavolcanics from the Malartic Composite Block intruded by felsic plutons. Zircon U-Pb ages of 2705±1 and 2706±3 Ma define the timing of the most recent phase of volcanism (Machado et al., 1991; Wong et al., 1991). The regional greenschist metamorphism has been constrained via $^{40}Ar/^{39}Ar$ dating to 2690-2675 Ma (Hanes et al., 1992).

The east-west trending Cadillac Tectonic Zone (CTZ) is located ~4 km south of Val-d'Or and constitutes a major first-order structure to which the faults and shear zones at Val-d'Or are considered subsidiary (Fig. 2.2) (Boullier and Robert, 1992; Sibson et al., 1988). While it has been suggested that the CTZ may have initiated as part of a normal or wrench fault system

(Dimroth et al., 1983; Hubert et al., 1984), the most recent movement has been shown to be reverse (Sibson et al., 1988). The CTZ separates the SAS from the metasediments of the Pontiac subprovince to the south which have been dated to maximum formation ages of 2691-2682 Ma (Neumayr and Hagemann, 2000). The CTZ likely acted as a major conduit from which auriferous hydrothermal fluids dispersed into subsidiary second and third order shear zones and faults, which host many of the deposits at Val-d'Or (Neumayr and Hagemann, 2000). Such deposits include the Sigma deposit (Robert and Brown, 1986b, 1986a; Sibson et al., 1988), the Lamaque deposit (Couture et al., 1994), and the recently discovered Triangle deposit (Dubé, 2018). Sigma, Triangle, and Lamaque are all quartz-tourmaline vein deposits that are concentrated within major, steeply south-dipping shear zones, and are spatially associated with large felsic intrusions (Couture et al., 1994; Dubé, 2018; Robert and Brown, 1986b).

Two sets of veins can be distinguished in the deposits at Val-d'Or (Boullier and Robert, 1992; Dubé, 2018; Robert and Brown, 1986b; Sibson et al., 1988). The first set contains steeply dipping veins—hereinafter referred to as steeps—typically located within the steeply dipping shear zones (Boullier and Robert, 1992; Robert and Brown, 1986b; Sibson et al., 1988). At the Sigma deposit, both the shear zones and steeps strike E-W and dip approximately 70° to the south (Robert and Brown, 1986b). The second set consists of subhorizontal veins (hereinafter referred to as flats), which at the Sigma deposit strike N-S and typically dip about 10° to the west (Robert and Brown, 1986b). Offset markers and corresponding wall geometries indicate that the flats at Sigma are hosted in fractures that are primarily extensional (Robert and Brown, 1986b). Rhythmic banding of tourmaline, quartz and carbonates within flats is characteristic and has been interpreted to indicate episodic opening events (Robert and Brown, 1986b). Regional fabric deflection along with offset and dragfolding of flats show that shear zones and faults are reverse to reverse-oblique (Boullier and Robert, 1992).

Steeps and flats are both continuous and mutually crosscutting structures throughout Sigma, implying a degree of contemporaneity between the sets (Dubé, 2018; Robert and Brown, 1986b; Sibson et al., 1988). Flats and steeps share similar mineralogies, with an average vein composition of 80% quartz, 15% tourmaline, and minor amounts of calcite, chlorite,

sulfides, scheelite and other accessory minerals (Robert and Brown, 1986a). Vein-quartz recrystallization, microfracturing of tourmaline within otherwise crystal-plastic mylonites, and dragfolding of flats indicate that the structures at Sigma were active at depths near the BDTZ (Boullier and Robert, 1992; Robert and Brown, 1986b; Sibson et al., 1988). This is a comparable depth to that of the greenschist-amphibolite transition, the proposed source of the hydrothermal fluids (Goldfarb and Groves, 2015; Scholz, 1988). Veins at Sigma contain inclusions with variable amounts of CO_2 located within healed microfractures in quartz (Robert and Kelly, 1987; Sherlock et al., 1993). Robert and Kelly (1987) suggest that the variability in CO_2 concentration is a result of CO_2 effervescence during rupture, and show that the auriferous hydrothermal fluid was low salinity, 15-30 mol% CO_2, and 285-395˚ C (Robert and Kelly, 1987). The lithostatic pressure was likely around 2-4 kbar (200-400 MPa) comparable to the base of the seismogenic zone in active systems (Robert and Brown, 1986b; Robert and Kelly, 1987; Sibson et al., 1988; R. H. Sibson, 1990).

The Lamaque mine is an open pit located 1 km south of Sigma and is hosted in greenschist-facies metamorphosed andesites and tuffs of the Val-d'Or Fm. that are intruded by calc-alkaline diorites and tonalites and tholeiitic diorites (Daigneault et al., 1982). Quartz-tourmaline-carbonate veins are exposed in the walls of the pit for hundreds of meters laterally and tens of meters vertically. The Triangle mine is an underground mine located about 3 km southeast of Sigma and is hosted in greenschist-facies metamorphosed tuff of the Val-d'Or Fm. that is intruded by diorites (Dubé, 2018). As at Sigma, quartz-tourmaline-carbonate veins at Lamaque and Triangle are hosted in south dipping shear zones with hydrothermal alteration envelopes (Daigneault et al., 1982; Dubé, 2018). Veins crosscut and occur within intrusions at both sites, and show variable degrees of crystal-plastic deformation (Daigneault et al., 1982; Dubé, 2018).

2.3 *Fault-valve behavior*

The fault-valve conceptual model considers a sealed, high-angle fault system in a compressive stress regime where the principal compressive stress components are $\sigma_1 > \sigma_2 > \sigma_3$

and where the plane containing σ_1 and σ_3 is vertical (Sibson et al., 1988). Fluids rising from the lower crust travel into the shear zone down pressure gradients (Sibson et al., 1988; Warren-Smith et al., 2019). As fluids infiltrate and migrate up the shear zone they encounter the impermeable base of the seismogenic zone and are trapped (Cox et al., 1987; Sibson et al., 1988). Impermeability at this depth may be due to solution transfer and hydrothermal mineralization sealing of fractures (Sibson, 2014). As fluids progressively accumulate at this level, pore fluid pressure ($P_{f)}$ increases. When P_f approaches the magnitude of the lithostatic load (σ_3) subhorizontal extension fractures open (i.e. $P_f > \sigma_3$). Due to the subhorizontal orientation of these fractures in a reverse faulting tectonic regime, P_f is only slightly relieved and may continue to rise at a rate which extension fracture generation cannot contend with (R. H. Sibson, 1990). These extensional fractures typically extend from faults, which has been interpreted to indicate that the faults are necessary pathways for the pressurized fluids (R. H. Sibson, 1990). Fault slip is initiated when both the regional differential stress and P_f are great enough so that the effective stress necessary for slip is reached (R. H. Sibson, 1990). At this stage, the rupture propagates towards the Earth's surface, immediately increasing fracture permeability and promoting fluid migration (Sibson et al., 1988). Shear stress is relieved, P_f is assumed to drop to hydrostatic levels, and a dramatic increase in permeability due to fracture allows for fluid infiltration (Sibson et al., 1988). Immediately following rupture it is believed that the hydrothermal fluid undergoes a phase separation associated with the sudden drop in pressure (Robert and Kelly, 1987; Sherlock et al., 1993). An exsolved gas phase is the first to infiltrate the newly formed open spaces in the faults and precipitates minerals (Fig 6) (Boullier and Robert, 1992; Sibson et al., 1988). Where fluids interact with freshly exposed wall rock, hydrothermal alteration occurs (Robert and Brown, 1986a). Minerals precipitate along the walls of opened fractures and grow towards the centers of the fractures (Boullier and Robert, 1992; Robert and Brown, 1986b, 1986a). Once fracture walls are completely mineralized, fluid-wall rock interaction ceases, also ending hydrothermal alteration of the wall rock (Robert and Brown, 1986a). Once faults and fractures have been fully mineralized and permeability is reduced, fluid pressure begins to rebuild again (Sibson et al., 1988).

2.4 *Field and Microstructural Observations*

Field observations were made at the Triangle and Lamaque deposits, but not at the Sigma deposit due to lack of preserved structures. Objectives included documenting the relative timing and orientations of structures and collecting samples of different lithologies for petrologic analyses. Due to the nature of the underground mine at the Triangle deposit, most exposures were no larger than 5m by 5m. Structures that were frequently observed at these deposits and of significance to this study are presented here. It was found that the Triangle and Lamaque deposits show similar structural frameworks to that described at Sigma (Robert and Brown, 1986b; Sibson et al., 1988).

The structures at Triangle and Lamaque exhibit a characteristic architecture comprising several inter-related elements. The host rock metavolcanics contain a regional foliation that dips in a range between 30-90˚. The foliation is defined by the alignment of platy minerals with flattened grains in between. Shear zones crosscut and deflect this foliation, and within their centers contain highly foliated mylonite. Steeps and flats at Triangle and Lamaque typically crosscut, though may also be deformed by, the shear zones, which are usually wider than the steep veins. The steeps and flats themselves crosscut each other, which has been interpreted to represent a mutually contemporaneous timing of formation. Veins may appear well-preserved or they may have undergone variable degrees of folding, stretching and boudinage. Flats always propagate outwards from steeps and may be dragfolded in a reverse sense. As has been described at Sigma, steeps and flats largely consist of mineral bands of quartz, tourmaline and carbonates (Boullier and Robert, 1992; Robert and Brown, 1986b, 1986a; Robert and Kelly, 1987; Sibson et al., 1988). The sides of tourmaline bands often show slickenlines that are subparallel to dip direction, which we have interpreted as slip surfaces.

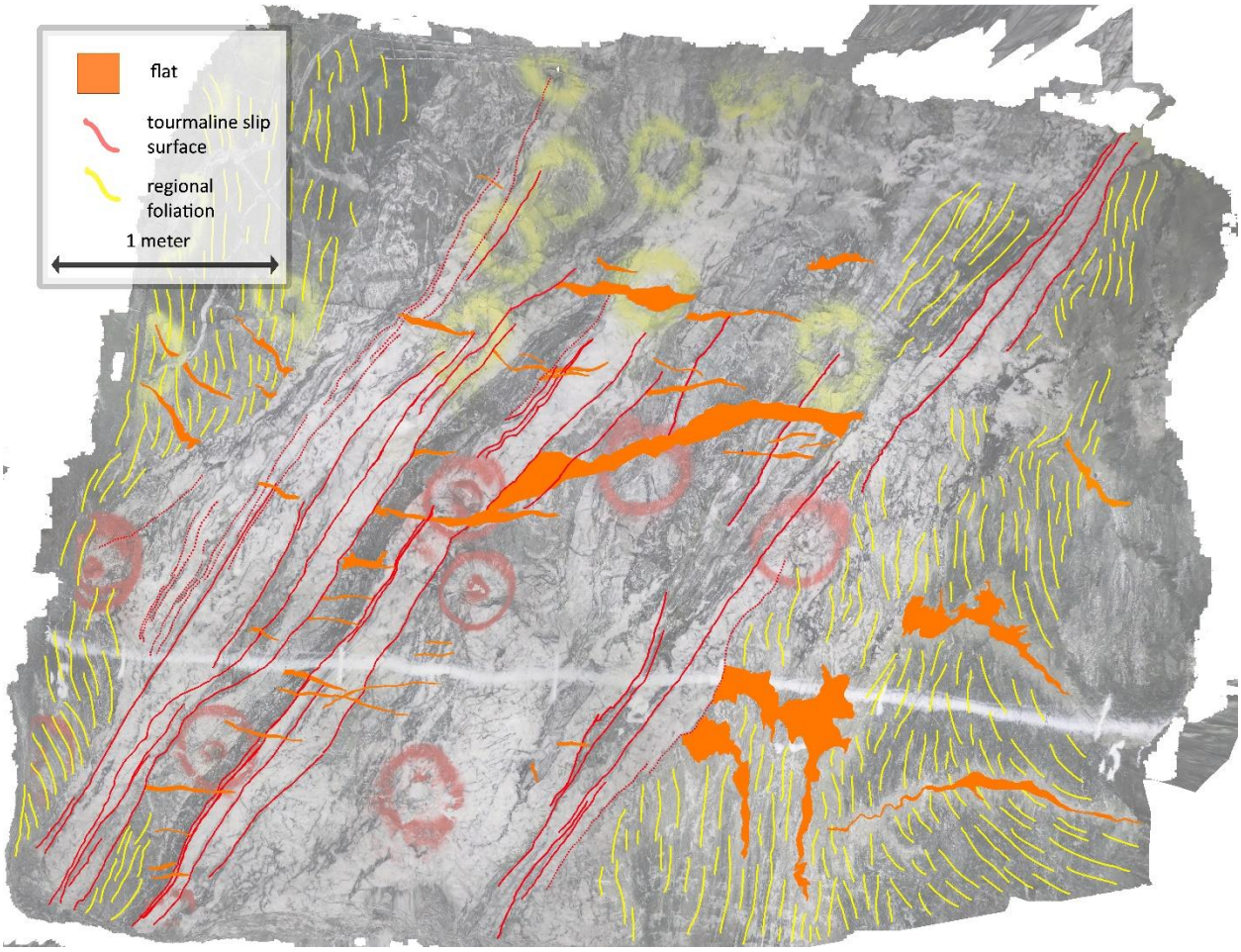

Figure 8. Annotated ortho-rectified image of stope wall in the underground Triangle mine, facing west at a depth of 202 m. Steeps consist of banded quartz (white), tourmaline (red lines) and carbonates (not labeled) along with lenses of wall rock. Flats show some drag folding in a reverse sense.

2.4.1 *Shear zones*

Crosscutting and deflecting the regional foliation are localized, E-W trending, south dipping zones of highly foliated rock that define shear zones (Fig. 2.2). Shear zones (n=24) have an average shear plane orientation of 109/49° S and shear zone thickness normal to the shear

plane ranges from 3cm to greater than 5m. Within shear zones, the regional foliation is deflected to form a sigmoidal shape consistent with reverse shear. In some instances, flats are dragfolded within shear zones showing reverse motion. Some boudins of quartz are accompanied by asymmetric sigmoidal strain shadows, which indicate a reverse sense of motion.

Veins located within shear zones are deformed to a variable degree; some veins are highly folded, boudinaged and contain finer grain sizes than neighboring veins, which are less ductily deformed or not at all. These observations are interpreted as older vein material recording greater crystal-plastic finite strain than younger, more pristine veins. Where shear zones deform the metavolcanic wall-rock, phyllosilicates are present in greater quantities in the shear zone than in rock more distal to the shear zone. These phyllosilicates are interpreted to be the result of hydrothermal alteration associated with vein mineralization.

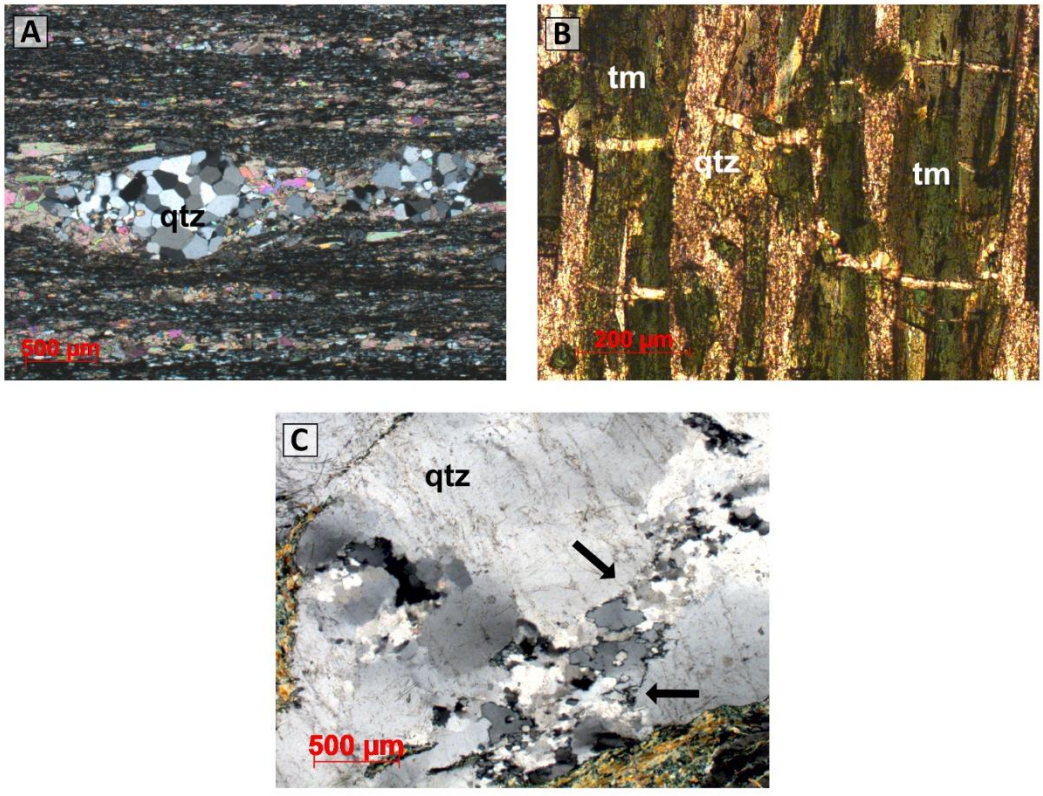

Figure 2.3. Photomicrographs showing representative mylonite microstructures. (A) Quartz pinch and swell structure within fine grained mylonite fabric that shows compositional banding.

Bands of different grain size and mineral types are apparent (cross-polarized light, XPL). (B) Microfractured grains of tourmaline (tm) within the mylonite. Quartz fills in the fractures. Plane-polarized light, PPL. (C) Bulging recrystallization in a quartz swell structure. Mantle of dynamically recrystallized subgrains surrounding a less strained core indicated by arrows (XPL).

Shear zones may contain fault rocks in which mineral banding at sub-mm scale defines a strong foliation, hereafter referred to as mylonites (Fig. 2.3). Mylonites developed from hydrothermally altered and unaltered metavolcanics, intrusions and vein material. All mylonite found in the field showed hydrothermal alteration, which is likely due to the fluid-conduit nature of the shear zones. Foliation within mylonites is most commonly defined by compositional banding of muscovite- and chlorite-rich layers separated by thinner quartz and feldspar layers. Where mylonite incorporates veins, quartz, tourmaline and carbonate grains are aligned with the foliation. Individual bands, in particular those made of quartz, may extend up to several meters. Quartz often forms irregular masses 1mm to 4cm thick around which all other minerals are aligned and deflected, indicating that quartz is one of the most competent mineral phases (Fig. 2.3 A). The exception to this rule is tourmaline, which only shows fracturing and around which quartz flows, making it the most competent mineral in the mylonite and veins (Fig. 2.3B). Quartz bands may also show boudinage or pinch-and-swell textures with boudins and swells up to 2cm long and 2cm apart (Fig. 2.3A).

Within quartz bands, grain sizes range between 600 µm to less than 10 µm. Quartz bands may be boudinaged or show pinch-and-swell textures and in these bands the grains are typically up to 600 µm. Quartz boudins and swells are typically accompanied by strain shadows with a sigmoidal shape, and within these strain shadows are relatively large grains of quartz, carbonate and albite that range between 40 µm to 600 µm. Quartz grains within strain shadows show bulging (BLG) recrystallization and the characteristic “core and mantle” texture (Fig. 2.3C) (Passchier and Trouw, 2005). Strain shadows have well-defined edges as the larger grains they contain are juxtaposed next to the mylonite matrix which contains much smaller grains that may be as small as 10 µm (Fig. 2.3A). Quartz bands show no apparent organization based upon their thickness; quartz bands with grains 500 µm wide and pinch-and-swell textures may exist

only 20 µm from quartz bands with 10 µm grains and consistent thickness. Based on the inferred variable finite strain and occurrence with alteration assemblage minerals, these quartz bands are interpreted as deformed vein quartz.

Similar to the quartz, calcite and dolomite form discrete bands which are also distinguished from each other by grain size. Carbonates form bands with grain sizes ~ 10 to 500 µm and grains are aligned with mylonite foliation. Carbonate grains greater than 100 µm often display twinning, and in some samples curved twinning is present. Grains of carbonate are also commonly found within the strain shadows of irregular quartz masses or pyrite clasts, ranging in size between 20-500 µm.

Cubic pyrite grains between 300 µm and 1mm long are common, have sharp edges, and sometimes are fractured. These pyrites are commonly accompanied by sigmoidal strain shadows that formed by rotation of the grains indicative of non-coaxial shear. Strain shadows contain grains of quartz, carbonates, chlorite and albite that may reach up to 500 µm in diameter.

Where vein minerals are not present in the mylonite, the foliation is defined by elongate grains of muscovite and blocky or elongate grains of chlorite. Chlorite may form grains up to 200 µm thick and 150 µm wide. Muscovite is typically platy and most commonly appears in bands 100-300 µm thick, although it may be dispersed throughout the mylonite fabric.

Rutile is dispersed throughout the mylonite as grains no larger than 15 µm. Apatite is also found throughout the mylonite, in small grains no larger than 15 µm.

Where tourmaline grains are found within the mylonite, they are elongate with lengths ranging between 20-500 µm, and often occur in bands 100-500 µm thick. Bands of tourmalines in mylonite contain extensional fractures up to 30 µm thick perpendicular to the foliation. These fractures only occur within tourmaline grains and do not extend into other minerals, and are sealed by quartz, tourmaline or calcite. Tourmaline is typically associated with quartz and carbonates in the mylonite, suggesting that it is vein derived.

2.4.2 *Steeps and Flats*

Vein dips at Val-d'Or show a bimodal distribution, with a cutoff between vein sets at 44° (Fig. 2.4A, B). Based on this distribution, veins with a dip between 0°- 44° are termed flats (n = 86) and veins with dips between 45˚-90˚ are termed steeps (n = 118). Steeps have a mean attitude of 114/56° S and a mean pole vector of 34˚/025 (trend/plunge). Flats have a mean attitude of 050/08° S and a mean pole vector of 82°/320. Steeps range in thickness from 3 cm up to larger than 5 m and flats range between 4-70 cm.

Field observations suggest the vein system initially formed contemporaneously with the shear zones and continued to form incrementally during brittle deformation. Flats and steeps exhibit mutually cross-cutting relationships with each other, and also exhibit varying degrees of ductile deformation. Steeps and flats may be stretched, folded and flattened to variable degrees and vein forming minerals (quartz, tourmaline, carbonates) are found in thin bands in the mylonite. In contrast, some veins are pristine, show no signs of ductile deformation, and may contain planar surfaces with slickenlines.

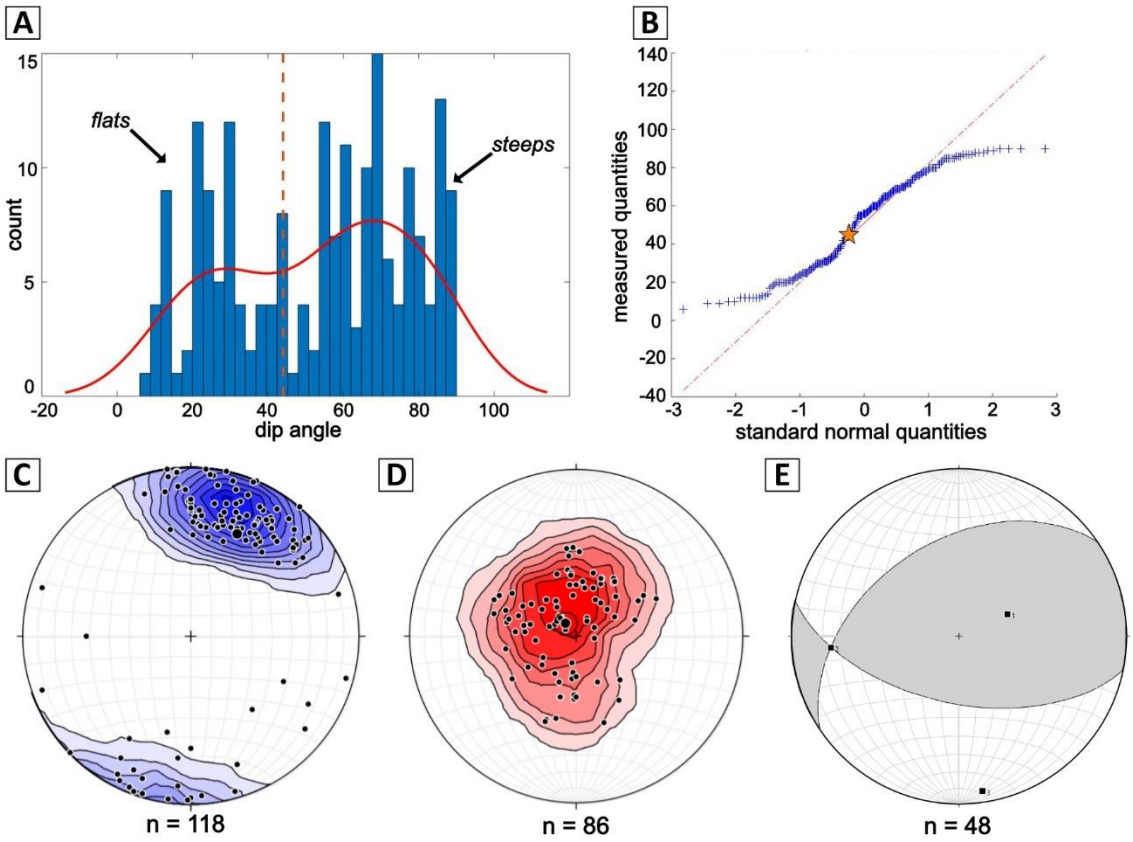

Figure 2.4. (A) The distribution of 204 measured vein dip angles. Bin count is 30. A probability density function is plotted in red, with the split point at 44 degrees in orange. (B) A QQ plot showing a normal distribution plotted against the measured vein dip distribution. The inflection point is at approximately 44 degrees. (C) Poles to measured steep attitudes at Triangle and Lamaque. Kamb contour intervals are 2 standard deviations. (D) Poles to measured flat attitudes at Triangle and Lamaque. Kamb contour intervals are 2 standard deviations. (E) Linked Bingham fault plane solution calculated using steep and flat rake measurements. Kinematic axes shown.

The majority of veins contain multiple bands composed of quartz, tourmaline or carbonate, which typically parallel vein edges and each other, although in many instances bands are truncated against others. Quartz bands are generally the thickest in any composite vein, ranging from less than 0.5 to ~50 cm thick. Tourmaline and calcite bands range in

thickness between less than 0.5 cm to 15 cm, although are mostly less than 5 cm thick. The maximum length of mineral bands in steeps was not observed due to limited exposure. Mineral bands in flats range from 1 to hundreds of meters long. Banding in flats and steeps did not typically display any continuity between them, instead showing mutually crosscutting relationships. Apparent offsets of bands within flats across steep veins was 1-15 cm in a reverse sense. Where mineral bands in flats intersect steeps or vice versa, they usually terminate into irregular brecciated masses.

Some of the mineral bands contain tourmaline crystals growing from the edges inwards, infilled by quartz. These tourmaline crystals occur as prismatic crystals up to 1 mm thick or as fibers that may be as narrow as 5 µm. These habits are interpreted to represent crystal growth in open space. Bands in which these textures are developed are typically 1-4 cm thick with tourmaline crystals or fibers 2 mm to 2 cm long. Whereas crystals typically grow perpendicular from vein edges, fibers often grow at an angle to the vein edges.

In steeps and flats, mineral bands of quartz, tourmaline or calcite may contain angular clasts of wall rock or tourmaline that define breccias. Breccia bands range between 2 - 20 cm thick and tens of cm to tens of meters long. Clast size ranges between less than 1 cm up to 10 cm. Most of the breccia bands are quartz bands containing fragments of the foliated, altered metavolcanics. Bands of tourmaline containing clasts of altered metavolcanics and bands of quartz containing calcite clasts also occur. These bands are part of the flats and steeps and exhibit a similar mutually crosscutting relationship with the other mineral bands.

All mineral bands in veins are interpreted to represent episodic opening and filling events, implying that veins are constructed intermittently over time. It was not possible to determine whether within any given vein if two bands were mineralized simultaneously.

2.4.3 *Tourmaline slip surfaces and stepovers*

Some of the tourmaline bands within both steeps and flats contain planar surfaces that cut across them or are located along their edges, which exhibit slickenlines (Fig. 2.5A, B). These slickenlines typically rake within 15° of the dip direction and appear as mm-deep grooves on

the tourmaline surfaces. Tourmaline-coated surfaces appear polished or in some cases have steps that are less than 1 mm high. In hand sample, small extensional microfractures less than 1 mm wide are visible, oriented subperpendicular to the dip direction. In many of these slip surfaces, the tourmaline exhibits a fibrous habit with fibers subparallel to slickenline orientation and dip direction, and subperpendicular to the extensional fracture set. Tourmaline slip surfaces crosscut the foliation, veins, and shear zones (Fig. 2.2, 2.5C). Where two or more parallel slip surfaces exist within the same vein, slickenline rakes may differ by up to 15°. This holds true even when parallel surfaces are only 2-5 cm apart. Slip surfaces are up to 50 m long and typically terminate abruptly within quartz.

The extensional microfractures that cut the fibrous tourmaline have apertures of 10-1000 μm and are observed to range in length between 40μm to several centimeters. These fractures are only present in tourmaline and are filled with tourmaline, quartz or calcite. In some instances, these microfractures show overgrowth of tourmaline or calcite along their walls, ranging from less than 2 μm to 20 μm thick.

Slip surfaces may step over or intermittently shallow in dip within the steeps to form dilational jogs during reverse slip. Slip across these dilational jogs, stepovers, or pull-apart structures, would have opened space for fluids to enter, acting as conduits for channelized fluid flow. Stepovers may overlap as little as 2-3 cm or as much as a meter, and their widths ranges between 1 cm to 50 cm. Stepovers may also underlap by as much as a little as 2-3 cm or as much as a meter, with a range in width of 2-35cm. Stepovers are filled with quartz, calcite and/or tourmaline. Tourmaline fibers grow across some of these dilational jogs, in the direction of the slip, perpendicular to fracture edges. Extensional fractures cut these fibers perpendicular to their long axes. Similar to the banding which occurs mostly in flats, banded minerals within dilational jogs are interpreted to record increments of slip.

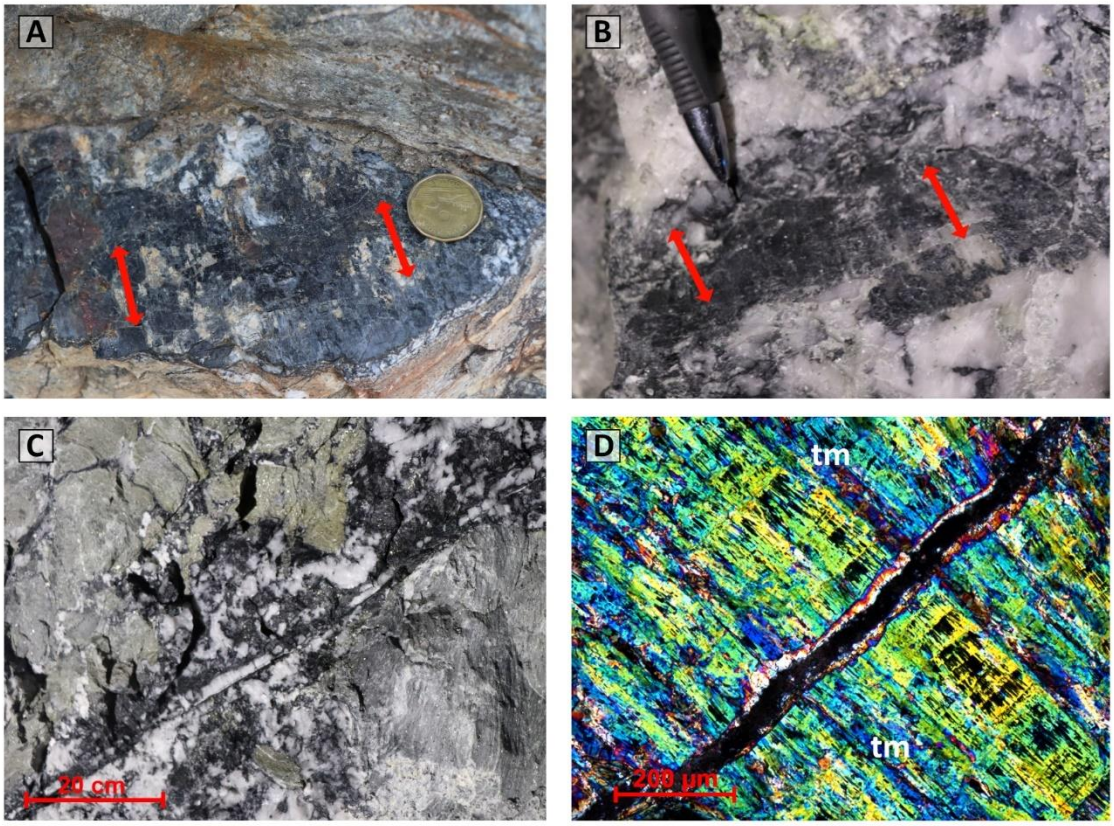

Figure 2.5 (A) Slickenlines on a tourmaline surface in a flat at Lamaque. (B) Slickenlines on a tourmaline surface in a steep at Triangle. (C) Facing underground tunnel wall with slip surface cutting through irregular vein material in a steep at Triangle. (D) Microfracture oriented subperpendicular to tourmaline fibers (tm). 10x, XPL.

2.4.4 *Hydrothermal alteration*

Zones of hydrothermal alteration envelope all observed steeps, flats and small carbonate veins. The alteration assemblage includes chlorite, muscovite, quartz, ankerite, K-feldspar, apatite, rutile, pyrite and chalcopyrite. Regardless of whether veins occur in metavolcanics or intrusions, the altered zones are always paler than the unaltered host rock. Alteration envelope thickness generally appears to increase with vein thickness, although this is not always the case as veins of different thicknesses may have envelope thicknesses of similar sizes. Where vein tips are present, alteration envelopes extend beyond the tips of veins. Altered

rock consisted of muscovite, chlorite, K-feldspar, carbonates, and minor apatite, rutile, and quartz.

Within hydrothermally altered mylonite, grains of muscovite up to 100 μm thick are observed overgrowing chlorite and are not aligned with the foliation.

2.4.5 *Relative Timing*

Based upon the structural observations described, the relative timing of the structures described above can be summarized as:

1. Regional foliation developed
2. Shear zones formed, deflected the regional foliation
3. Faults formed while shear zones are still active. Veins began to form.
4. Mixed continuous-discontinuous deformation as aseismic shear zones and episodic fault rupture occurred contemporaneously. Veins record this deformation.
5. Shear zones became inactive, faults remained active. Veins continued to grow.
6. Faults became inactive. Vein formation ended.

2.5 *Analyses and Tests*

2.5.1 *Tourmaline thermometry*

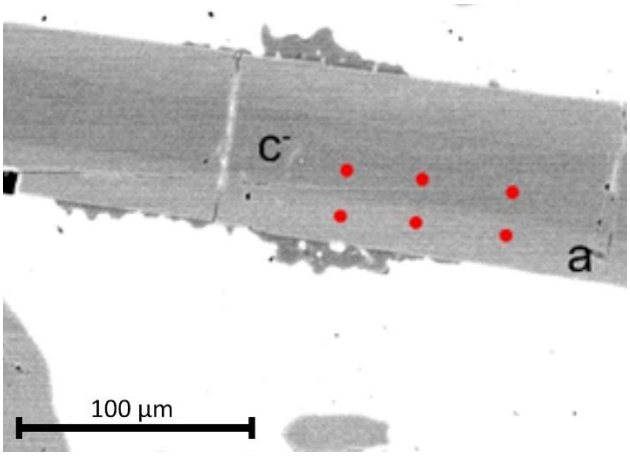

Figure 2.6 Backscatter electron image of a zoned tourmaline crystal. The c- and a sectors are labeled, and red points indicate where compositions were measured.

The degree to which Ca, Ti and a host of other major and trace elements fractionate between sectors in metamorphic tourmalines has been shown to be temperature dependent (Hinsberg and Schumacher, 2007). The tourmaline structure includes Si tetrahedral rings which all point in the same direction, giving it a noncentral symmetry. The asymmetric structure of tourmaline produces crystals with dipolar surface charges and compositionally distinct sector zones (Henry and Dutrow, 1992). Cations with higher charges will be enriched in the c- sector of the tourmaline crystal as they are preferentially incorporated on the negatively charged c- growth faces, while cations with lower charges, and vacancies will be higher in the c+ sector (Henry and Dutrow, 1996; Hinsberg and Schumacher, 2007). The composition of the a-sector is not affected by this dipolarity, as its growth surface is perpendicular to the dipolar charge (Hinsberg and Schumacher, 2007). At higher temperatures, the polar surface charges decrease due to the increase in vibrational energy and increasing the flexibility of bond lengths and angles in the tourmaline structure, which diminishes the fractionation among the sectors (Hinsberg and Schumacher, 2007). Using the empirical calibrations from van Hinsberg and Schumacher (2007), temperatures between 300-650˚C can be determined from the fractionation of Ca and Ti between sectors in individual tourmaline crystals [2,3] (Henry and Dutrow 1992, 1996; Sperlich 1990; Sperlich et al. 1996; van Hinsberg and Schumacher 2006).

Five thin sections were selected for tourmaline thermometric analyses. Sample NO18-06 contains tourmalines from a slip surface in the Lamaque pit, samples NO18-112B and NO18-102 contain tourmalines from within a pull-apart structure and vein breccia, respectively, from the

Triangle mine, and sample S4 contains tourmalines from slip surfaces within the Sigma mine, collected during a previous study. The preservation of both the tourmaline-bearing brittle structures and the sector zoning within the tourmalines indicates these samples have undergone little to no deformation or compositional modification since their formation and likely formed in the latest stage of deformation(Büttner and Kasemann, 2007). Tourmalines in S4 and 112B contain microfractures which generally cut the fibrous crystals perpendicular to their long axes.

Two types of sector zoning were observed in the tourmaline grains; complementary polar overgrowths on fracture surfaces and hourglass sector zoning. The hourglass sector zoning can be identified in samples in microscopy by color. The *c-* sector is characterized by a blue hue, whereas the *a* sector is green and the *c+* sector is brown. SEM backscatter electron images were then used to confirm the compositional differences between these zones. In order to distinguish the hourglass sector zoning from regular growth zonation we took into account the geometry of the sectors and consistency of the fractionation of the elements among the sectors. Polar overgrowths were found to be too small to measure by microprobe, and therefore all measured points are associated with intersector zoning. Points were measured in pairs to determine the relative concentrations of cations (including Ca and Ti) in *c-* and *a* sectors or *c+* and *a* sectors (Fig. 2.6). The points were positioned close to the edges of the sectors to ensure that points from each pair were complementary in terms of growth timing. 2-4 pairs of points were measured along each sector boundary to determine how consistent the fractionation was. Sectors from 1-5 crystals were measured in each thin section for a total of 60 points. Since tourmaline only occurs within the veins, its formation is directly tied to the presence of hydrothermal fluid. The tourmalines are therefore inferred to record temperatures at which fluids were traveling within the veins during mineralization.

Chemical analyses were conducted on a Cameca SX Five FE microprobe at McGill University, Quebec, Canada. The operating conditions were a 20 nA beam current at 20 kV accelerating voltage with a beam width of 3 µm. All standards used were from the C. M. Tayler set. Fluorite was used to calibrate F, Diopside was used to calibrate Si, Mg, Ca, Albite was used to calibrate Na, Sanidine was used to calibrate Al, K, Rutile was used to calibrate Ti, Magnetite

was used to calibrate Fe, Spessartine was used to calibrate Mn, and Chromite was used to calibrate Cr. A ZAF correction was applied to all analyses, taking fixed concentrations of B_2O_3 (10%) and H_2O (2.5%) into account. Average detection limits for each major element were F 1389 ppm, Na 342 ppm, Si 115 ppm, Mg 129 ppm, Al 209 ppm, K 65 ppm, Ca 71 ppm, Ti 83 ppm, Fe 197 ppm, Mn 145 ppm, and Cr 122 ppm.

Weight percentages of the major oxides measured at each individual point were converted to cpfu (cation per formula unit) values using a normalization factor of Y+Z+T (sites within the crystal lattice) cations = 15. The cpfu ratios for *a*/*c*- and *a*/*c+* pairs were then calculated—these are the Intersector D values. Ca and Ti prefer the c- sector over the a sector, and prefer the a sector over the *c+* sector. To calculate temperatures for *c*-/*a* sector pairings, D values for Ca (D_{Ca}) were input equation 2.1 and D_{Ca} values for *c+*/*a* pairings were input into equation 2.2.

$$T = (-0.004284 \langle\langle \ln(D) \rangle\rangle^3 - 0.007346 \langle\langle \ln(D) \rangle\rangle^2 - 0.004436 \ln(D) + 0.001449)^{-1} \quad \text{(Eq. 2.1)}$$

$$T = (-0.00063236 \langle\langle \ln(D) \rangle\rangle^6 + 0.014565 \langle\langle \ln(D) \rangle\rangle^5 - 0.040638 \langle\langle \ln(D) \rangle\rangle^4 + 0.037474 \langle\langle \ln(D) \rangle\rangle^3 - 0.014321(D)^2 + 0.0037503 \ln(D) + 0.0015393)^{-1} \quad \text{(Eq. 2.2)}$$

These equations are best fit curves through empirical tourmaline intersector partitioning data from van Hinsberg et al. (2007) that assume a 1/T vs ln(K) relationship and are extrapolated down to 200˚C. D values obtained from Ti measurements were not used since Ti should only be minimally soluble at these temperatures. Ti concentrations will not represent equilibrium between sectors and will therefore provide minimum estimates of temperature.

The mean temperature calculated from all compositional data is nearly equivalent with the temperature calculated from the ratio of the mean a-sector composition to the mean c or c-sector composition. Also, although individual samples gave temperatures that varied by up to

hundreds of degrees, the median temperatures for all samples from Lamaque and Triangle were in agreement (Fig. 2.7). These observations suggest that the spread in temperature is an effect of noise in the data more so than a true spread in temperature. Sample S4, which is from the Sigma mine, clearly reflects a lower temperature fluid, perhaps from a different generation or source.

The calculated median temperatures for NO18-06, NO18-102, NO18-112B, and S4 are 312˚C, 298˚C, 313˚C, and 209˚C, respectively (Fig. 2.7). The temperature calculated for S4 clearly reflects a lower temperature fluid at Sigma, while the samples from Lamaque and Triangle show similar temperature estimates. The average temperature of samples from Lamaque and Triangle is 308˚C.

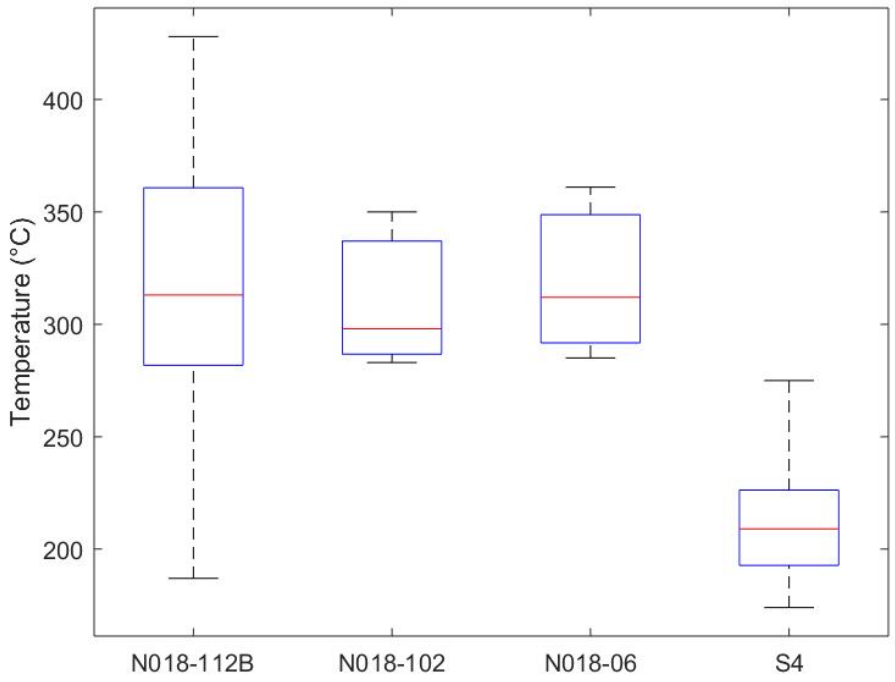

Figure 2.7 Box and whisker plots showing tourmaline thermometry results. Red lines indicate median temperatures, bottom and top edges of each box indicate the 25th and 75th percentiles, respectively, and whiskers extend to the furthest outlier temperatures. Sample S4 is from Sigma, while samples NO18-06 is from Lamaque, and NO18-102 and NO18-112B are from Triangle.

2.5.2 Tourmaline tensile tests

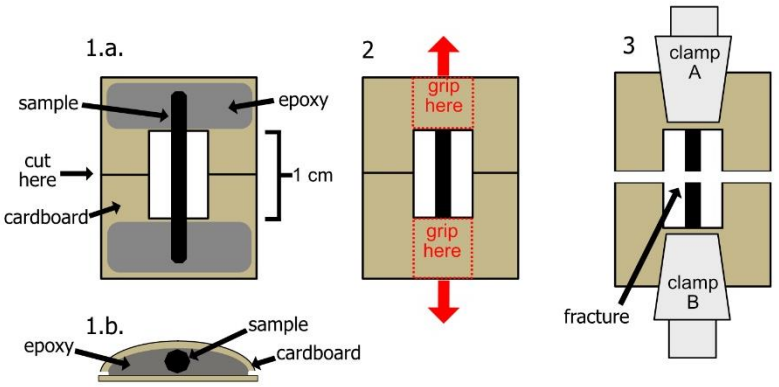

Figure 2.8 Schematic of tensile experiment design. 1.a.) An exposed view of the sample (black) with cardboard frame beneath (brown). The tourmaline crystal is epoxied (grey) to a cardboard frame with a window that is 1 cm long in the direction parallel to the crystal's long axis. 1.b.) View looking down the long axis of the crystal. Note that sample is epoxied between two cardboard frames, and that one of the frames is folded around the sample while the other is flat, which helps improve the clamp hold. 2) Grip locations for clamps shown along with extension direction during the tests. Cardboard is cut along black lines in middle of frame. 3) Clamp B is stationary while clamp A moves away.

Since tourmaline fibers are observed to parallel the slip direction as defined by slickenlines and are perpendicular to extensional microfractures, we interpret the them to have stretched and failed in tension during slip along the fault. Stepovers where the slip surface temporarily shallows in dip act as extensional jogs during reverse slip and within these jogs tourmaline fibers may stitch the two sides together, with their long axes parallel to the slip direction. Due to the geometric relationship between the tourmaline fibers and fault slip direction, we equate the tensile strength of tourmaline to the shear stress resolved on the fault to cause slip.

In order to determine the tensile strength of tourmaline, we conducted a series of tensile tests. The theory behind tensile tests is described in detail by Hart (1967). A set of 10 compositionally homogenous commercially available tourmalines were pulled apart along their long axes at room temperature (15˚C) using a UniVert Cellscale (Fig. 2.8). The Cellscale stretches a sample vertically between two sample holders while measuring the force required. To ensure

the elongate crystals were loaded with vertical long axes, 3cm x 3cm cardboard sample holders with 1cm x 1cm windows in their centers were constructed. Individual tourmaline crystals longer than 1cm were sandwiched between two carboard frames with the crystal edges aligned with the interior widow edge. The crystals were attached to the cardboard with epoxy resin, which bonded to both the crystal and the cardboard, effectively increasing the cross-sectional area of the tourmaline where the epoxy was attached. An extension rate of 0.02 mm/s was applied to samples until fracturing in tension occurred. The same starting conditions were applied to all tests.

In order to convert the measured tensile force into a traction value, the surface area of the fracture in each sample was measured. Photographs were taken oriented normal to the fracture surface and the software ImageJ was used to compute the surface area. A hand drawn outline of sample T10's fracture surface perimeter was made, and the area of this drawn perimeter was then determined for comparison to the surface area measurement. The drawn area was found to be within 0.04 mm^2, which is ~1% error. Crystals appeared to break at an elongation of about 1%. Visual assessment of the fracture surfaces showed no inclusions within the fracture face.

A range of tourmaline tensile strengths were measured, from 9 to 44 MPa. Since small pre-existing microfractures or geometric anomalies in the cross-sectional shape of a sample may result in a lower tensile strength measurement, the largest tensile strength measurement is the most useful value for homogenous tourmaline in the fault. Sample T10 gave the greatest tensile strength value, which was 44 MPa (Fig. 2.9).

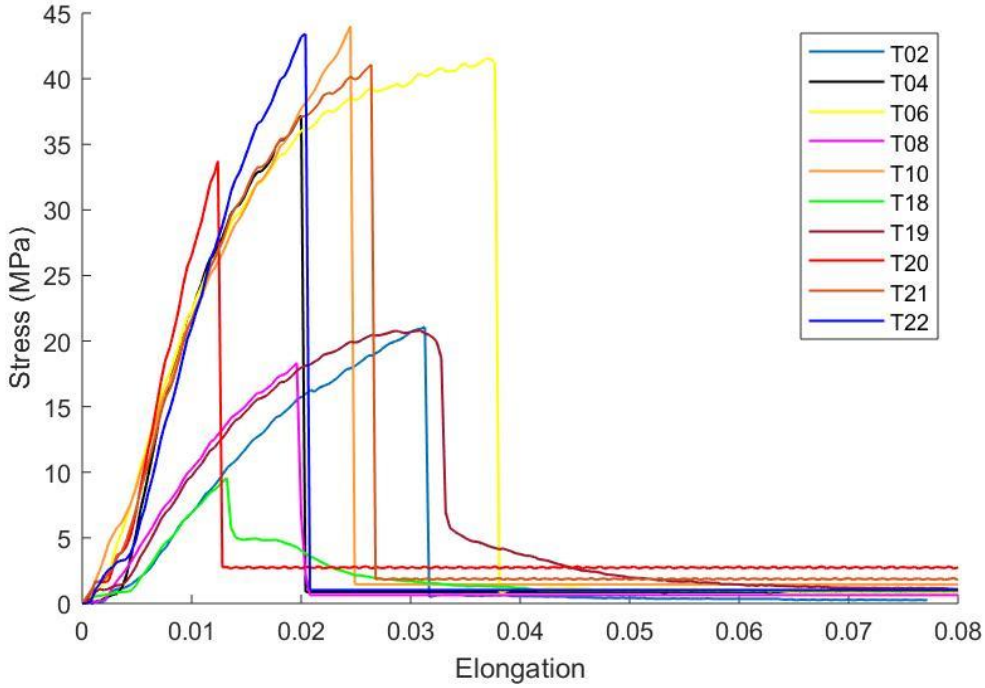

Figure 2.9 Tensile test results for all samples. Sample T19 fractured within the epoxy, which is likely responsible for the non-abrupt stress drop.

2.6 *Discussion*

2.6.1 *Tensile test results*

Tensile test results show that samples progressed through three deformation regimes during the test. At small extension, all samples appear to undergo an initial nonlinear phase, which is interpreted to be a result of the clamps adjusting to the epoxy-cardboard sample holders. A clear linear regime follows during which the sample stretches elastically. Just before failure, samples again undergo a non-linear phase, potentially due to crack nucleation and coalescence prior to macroscopic failure. Most of the samples fractured within the crystals, away from the epoxy holds, and so the peak forces measured must be a function of the tourmaline tensile strength.

Kimura et al. (2006) measured the tensile strength of tourmaline at room temperature using the three-point bending test method and provide a fracture strength estimate for tourmaline of 110 MPa. These results were considered representative for tourmalines in the

upper crust, assuming that as a silicate mineral tourmaline would not experience a great loss in strength until reaching ~ 600˚ C (Kimura et al., 2006). Higher confining pressures in creep tests have been shown to increase the time to failure and amount of plastic deformation a rock can maintain before becoming unstable, although this has been attributed to the presence of cracks along grain boundaries and joints (Kimura et al., 2006; Kranz, 1980). Kimura et al. (2006) consider pressure to have little effect on tensile strength, asserting that tourmaline crystals should not contain any of these preexisting cracks.

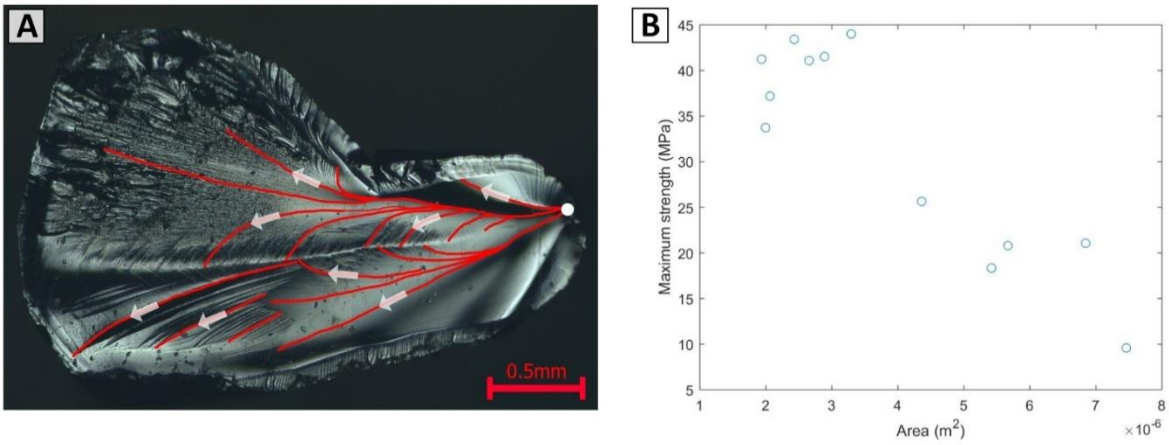

Figure 2.10 A) Fracture surface from sample T10. Hackle marks are traced in red, with inferred direction of fracture propagation shown by arrows. B) Strength appears to scale with cross sectional area, which may be due to a greater probability of imperfections with great cross-sectional area.

The discrepancy between our maximum strength estimates and that provided by Kimura et al. (2006) may be explained by small geometric irregularities and/or pre-existing microfractures within the tested crystals. Many of the fracture surfaces produced during tensile testing contain plumose structures (Fig. 2.10A). Twist hackles are also observed in many of these fracture surfaces (Fig. 2.10A). Many of the plumose structures on fracture faces converge to small areas that indicate fractures nucleated at corners or geometric irregularities along the edges of the crystals, which alongside the occurrence of twist hackles we interpret as signs that the geometry of the crystal resulted in locally concentrated stresses. An example is sample T10, in which a plumose structure nucleates at the edge of the grain (Fig. 2.10A). Irregularities in the

crystals should result in local stress concentrations that effectively lower the maximum peak strength required to cause fracturing (Griffith, 1921). Strength values obtained from tensile testing can be grouped into a stronger and weaker set (Fig. 2.7, 2.10B). One set shows peak strength values near 35-44 MPa while the other set shows peak strength values near 25-20 MPa. The stronger set had lower cross-sectional surface areas than the weaker set (Fig. 2.10B). This correlation may be explained by larger crystals having a greater likelihood of containing preexisting microfractures, which would lower the applied stresses necessary for failure. The relationship between tourmaline grain cross-sectional areas and tensile strengths follows a linear trend (Fig. 2.10B). Projecting this trend to cross-sectional areas of 10^{-10} m^2 for 10 μm diameter crystals suggests a moderately higher tensile strength around 53 MPa.

Given that these effects are significant, but that natural crystals within the studied slickenside surfaces would also be imperfect, we propose that our estimates give a minimum tensile strength magnitude for the structures at Val-d'Or, while the estimate given by Kimura et al. (2006) (110 MPa) provides an upper estimate.

2.6.2 *Constraints on the fault valve model*

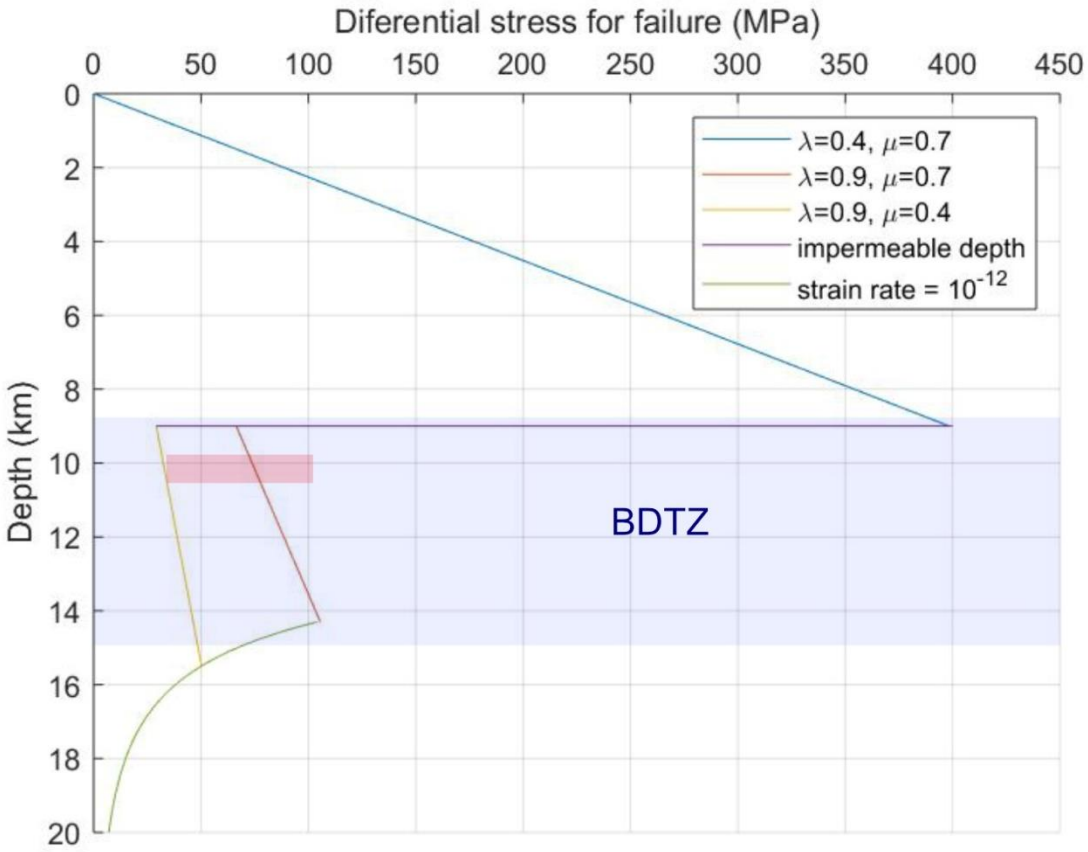

Figure 2.11 Modified strength profile of a fault with a 60˚ dip with a high pore pressure zone (orange) beneath an impermeable depth. Estimated fault-valve model depths and stresses shown in red. Strength in the ductile regime is shown by the flow resistance of quartz (green). The range of the box is set by depths calculated using a geothermal gradient of 30 C/km and a temperature range of 298-313 C determined from tourmaline intersector thermometry.

The observed geometry and kinematics of the tensile cracks perpendicular to the fibrous tourmaline crystals aligned with slickenlines allow us to place constraints on stress magnitudes for the faults at Val-d'Or. Using our maximum tourmaline tensile strength measurement (44 MPa) as a proxy for the shear stress (τ) resolved on the fault during slip, we calculate the corresponding differential stress (σ_d) using the Mohr equations. We consider faults with dips of 70˚ (the mean shear vein dip at Sigma given by Sibson et al. (1988)), 60˚, and 56˚ (our mean steep dip). σ_d estimates for these faults are 105 MPa, 51 MPa, and 35 MPa, respectively. These results agree with the assertion put forth by Sibson (1990) that the magnitude of σ_d in severely misoriented faults should not exceed tens of MPa.

The magnitude of differential stress calculated above can be contextualized by determining the depth of faulting as a constraint on the absolute stress magnitudes. As summarized in Section 2.4.5, crosscutting relations indicate the plastic structures formed early in the deformation history, followed by the brittle structures, consistent with an overall retrogressive change in conditions during deformation. Considering a geothermal gradient of 30˚C/km and the deformation temperature range of 298-313˚C obtained via tourmaline thermometry on samples that exhibit the tensile cracks oriented perpendicular to slickenlines, we conclude that these fractures and the mineralization that filled them occurred at ~ 10 km depth. Jébrak et al. (1991) found the density of country rock in the region to range between 2.65-3.00 Mg/m^3. Calculating for a vertical pressure gradient using this density range gives a pressure gradient range of ~26 to 30 MPa/km. At 10 km, this corresponds to a lithostatic stress (σ_L) range of ~260-300 MPa.

Frictional failure under differential stress of tens to 100 MPa at these depths requires very high pore fluid factors ($\lambda \approx 0.9$) and an effective coefficient of friction (μ) between 0.4 and 0.7, values lower than typical for crustal rocks (Fig. 2.11) (Byerlee, 1978). Implicit in the conditions required for fault-valve behavior is an impermeable barrier that allows pore fluid pressure to build up toward lithostatic values, which Sibson has recognized as the base of the seismogenic zone (Sibson et al., 1988). A modified crustal strength diagram with a consistent $\mu=0.7$ and with $\lambda=0.4$ above the impermeable depth (and $\lambda=0.9$ beneath the impermeable depth) is shown in Figure 19. Due to the very low effective stress conditions implied by our data, the composite strength profile has a particularly weak midcrustal layer near the base of the seismogenic zone within which sealing conditions and fluid overpressures due to metamorphic dewatering reactions play a significant role.

The kinematic inversion of the steeps attitudes and slickenline directions gives non-vertical axes (Fig. 2.4E). If these axes approximate the principal stresses during deformation, they imply non-Andersonian conditions, which is counter to typical expectations for stress field orientations. This may be explained by rotation of the vein system post-vein formation. While it is not known if or how much rotation post-vein formation may have occurred, rotating our

structural measurements so that the mean flat orientation has a vertical pole does not set the kinematic axes to be aligned with the vertical and horizontal directions. Other assumptions necessary to relate the kinematic inversion to a corresponding stress field include minimal rotation of the faults during slip, that the slip occurred in a single phase of deformation, and that the slip direction recorded by slickenlines occurred in the direction of maximum resolved shear stress. We have no direct constraint on fault rotations, although the shear zones, steeps and tourmaline slip surfaces are all roughly parallel. Overall, since we do not have direct constraints on the paleostress orientations, we assume a simplified framework with Andersonian principal stress directions during vein formation followed by subsequent rotation of the system.

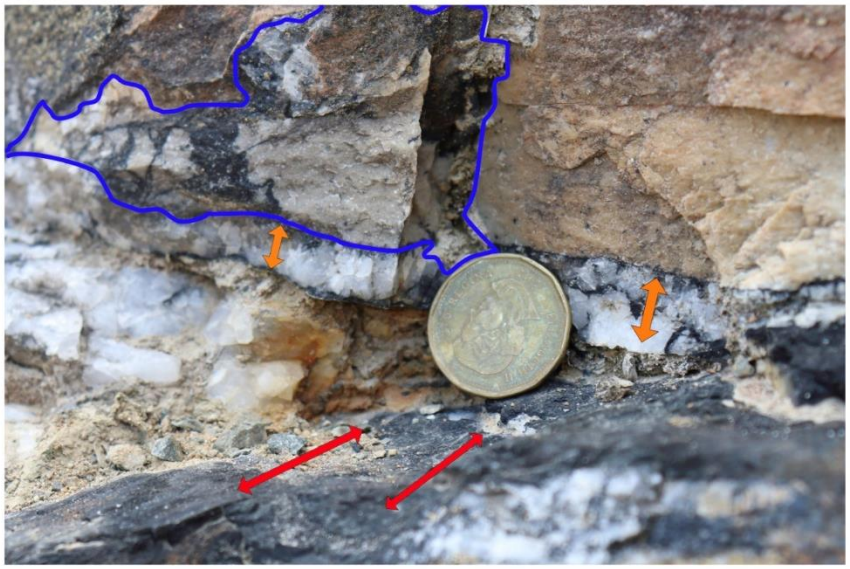

Figure 2.12 Flat at Lamaque containing slickenlines on a tourmaline surface (red arrows), open growth texture (orange arrows), and breccia (blue). Coin for scale.

Flats at Sigma have been interpreted to record episodic extensional fracturing (Boullier and Robert, 1992; Sibson et al., 1988). However, slickenlines within the flats at Triangle and Lamaque indicate that some component of shear was resolved on these surfaces. This is further complicated by the observation that many flats contain slickenlines and open-growth textures together (Fig. 2.12). Additionally, individual veins may contain multiple parallel slip surfaces with rakes that differ by up to 15˚. We attribute shear in the flats to be a result of irregular flat

geometry, and the coexistence of extensional bands and slickenlines to changes in the geometry of the fracture over the course of subsequent slip events. The different slickenline orientations within a single vein may be a result of changing stress orientations throughout vein formation. The precise shear direction (i.e. normal or reverse) in the flats could not be determined via any kinematic indicators, however by assuming reverse slip in the flats we can produce kinematic axes and a fault plane solution that is nearly identical to those produced by plotting reverse motion in the steeps. We therefore interpret reverse motion is responsible for the slickenlines present in the flats. Changes in the stress field orientation may also explain the observed coexistence of extensional bands and slip surfaces within a single vein. Also of note is that most flats do not show horizontal orientations, even after backrotating all measurements to give a mean flat orientation that is horizontal. Shear in these non-horizontal flats may have produced the slickenlines observed, and the progressive evolution and slip of non-horizontal veins with irregular geometries may explain the occurrence of open growth textures and slickenlines together.

Boullier and Robert (1992) have shown evidence of reversals in the maximum and minimum principal stress directions during fault-valve behavior at Sigma As P_f decreases after rupture, the overburden causes flats to collapse, resulting in a transient stress reversal (Boullier and Robert, 1992). This indicates that upon rupture, τ dropped to at least near 0 MPa and likely lower than 0 MPa. While the lower bound of the stress drop is not constrained, the transient nature of the stress reversal suggests that it does not reach much lower than 0 MPa. For the average fault dip in reported here of 56˚, a total stress drop equates to $\Delta\tau$ = 44 MPa.

Upon rupture, slip on the fault opens spaces at dilational jogs causing P_f to drop from lithostatic levels down to a minimum buffered by the fluid-vapor equilibrium pressure (P_E). This is because the diffusion of fluid pressure through relatively impermeable rocks is unable to keep up with the rapid increase in fluid volume caused by slip, and the associated pressure drop results in decompression boiling. At this point, a vapor phase will separate and be the first to occupy the newly formed pore space, while the fluid will lag temporarily. P_E is the pressure at which both the fluid and vapor phases are in equilibrium and will be lower than the hydrostatic

pressure (P_H). Eventually the pressure will climb up to P_H and subsequently higher if the flux of fluid and fault seal are maintained. In order to calculate the pressure drop which results in the phase separation, the XSteam Tables module for MATLAB (Holmgren, 2006) was used to calculate P_E. For saline solutions, P_E is given by the vapor pressure of the pure solvent multiplied by the molar fraction of NaCl (Raoult's law) (Williams, 2019). Robert and Kelly (1987) estimate that the hydrothermal fluid at Sigma has a composition of <10 wt% NaCl. Based on the results of our tourmaline thermometry, we take 308˚ C as a deformation temperature. Considering a hydrothermal fluid with 1-10 wt% NaCl at T=308˚ C, our estimated P_E is 9-10 MPa.

P_E will be lower than P_H, as it is the pressure at which both a vapor and fluid phase coexist at our given temperature. As shown in Fig. 2.11, P_f must have been ~$0.9\sigma_L$ at the initiation of slip. P_H at ~10 km depth would be ~100 MPa. The pressure drop (ΔP_f) is given by $\Delta P_f = 0.9\sigma_L - P_E$. Given our estimated σ_L (258-307 MPa) and P_E (9-10 MPa) ranges, our estimated ΔP_f range is 222-267 MPa. This pressure drop will be local to the dilational sites in the fault and will exist transiently until pore pressure diffusion and/or flow into the jog can re-equilibrate P_f. It should be recognized that our estimated σ_L range reflects the maximum depth at which brittle deformation is occurs, as it is calculated using the deformation temperature calculated from tourmaline intersector zoning. Mineralization and frictional slip will occur above this depth (at lower magnitudes of σ_L), but not necessarily below. Additionally, P_E is a lower bound on the vapor-liquid equilibrium pressure. Our calculation assumes that fluid pressure is buffered by steam, but other factors (i.e. mineral growth and fluid flow rates into the newly opened spaces) could affect this value.

As noted by Sibson (1985), a relatively dry BDTZ ($\lambda \approx 0.4$) would require very high differential stress magnitudes for failure (Fig. 2.11). The presence of overpressured fluids (and a high pore fluid factor) dramatically weakens the shear strength of structures in the BDTZ. In all samples of tourmaline slip surfaces collected and analyzed, tourmaline crystals are either intact or fractured, and nowhere do tourmaline grains appear to have been deformed plastically (although boudinaged tourmalines appear in mylonite). Although the aperture of healed extension fractures and mineral bands are relatively small and the associated slip would also have been small, we infer these slip events would have been earthquakes (Boullier and Robert,

1992; Cox, 2016). This suggests that mineralization and deformation in veins was occurring above the base of the seismogenic zone if the seismogenic zone is defined as the region of a fault where earthquakes nucleate. Our results show that the shear strength of the faults during deformation was of the order of tens of megapascals. Intersection of the frictional failure curves at high pore fluid pressures with the quartz flow law suggests that at least part of the relatively weak BDTZ (Fig. 2.11). Since fault-valve behavior at Val d'Or is spatially associated with the base of the seismogenic zone, our results suggest that this that the base of the seismogenic zone can also be weak. This weaker, saturated section of the BDTZ is capped by the impermeable barrier, above which pore fluid factor values are low. Some impermeable barrier is necessary to generate high pore fluid pressures, and at the base of the seismogenic zone impermeability is believed to be sustained through the mineralization of fractures around 150-300˚C. The depth at which hydrothermal fluids will mineralize is controlled by a broad suite of parameters, the most significant of which is likely temperature (Hill, 1992; Sibson, 2014; Völker et al., 2011). A warmer crust may allow for mineral sealing of faults and fractures at shallower depths, which could explain a shallow base of the seismogenic zone at locations like the Long Valley Caldera (Hill, 1992).

The numerous tensile fractures that cut the tourmaline slip surfaces indicate a large number of repetitive slip events occurred on the faults in the Triangle mine. We infer from the field and microstructural observations that these slip events were small magnitude because the apertures of the tensile fractures are limited to mm or less. In addition, most mineral bands in flats in the Triangle mine have thicknesses of order of a few centimeters or less, which records opening in flats and potentially slip on steeps. This qualitative assessment of the slip increment size suggests that most of the earthquakes that occurred in the past at Val d'Or were small and of similar magnitude. This would support the notion by Cox (2016) that earthquake swarms—characterized by many small but similar magnitude events—could be explained by fault-valve behavior. An example of a modern case of fault-valve behavior is the 2004 Mid-Niigata Prefecture sequence was comprised of a M_J6.8 mainshock and rich aftershock sequence which included 3 M_J>6.0 events over 3 days at 7-12 km depth, across both optimally oriented and misoriented faults in a compressive regime. Sibson (2007) asserted that the reactivation of both

the optimally oriented and misoriented faults would have required large degrees of fluid pressure cycling, and thus suggests Niigata as a modern analog for fault-valve behavior (Sibson, 2007). By quantifying the stress and pore fluid pressure variations in the Triangle-Lamaque deposits, our results emphasize that swarm-like behavior may result from slip under very low effective stress conditions due to fluid percolation along fault surfaces that cut low permeability host rocks, which trap, or channelize fluid flow.

Chapter 3 – Conclusion

3.1 *Conclusion*

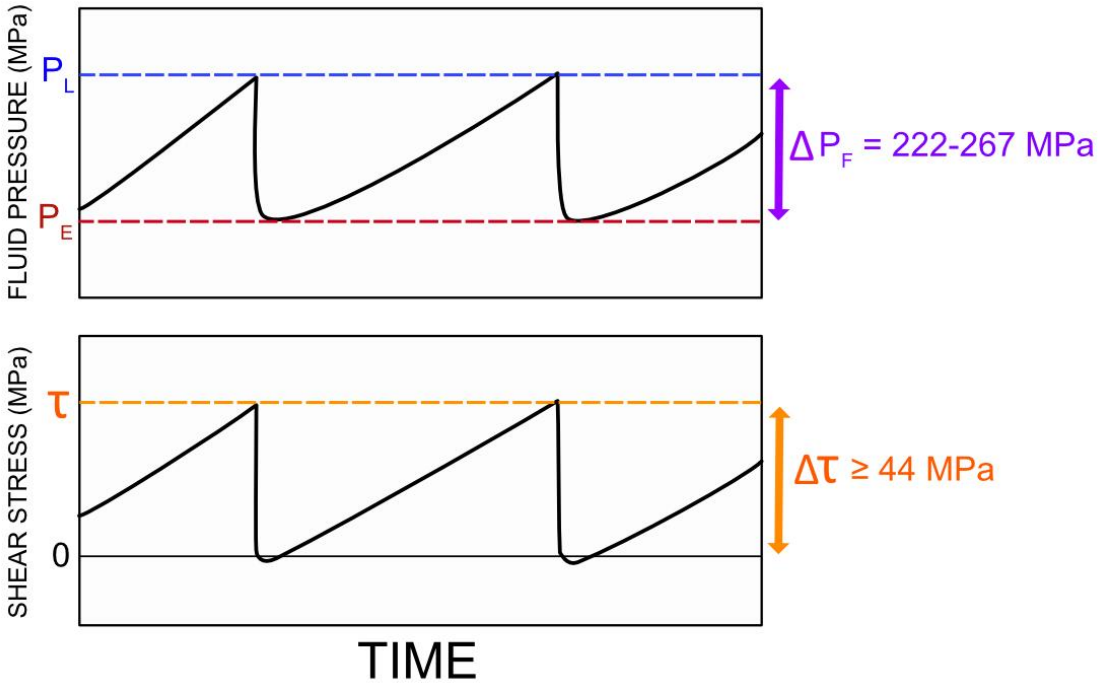

Figure 3.1 Pressure and stress cycling constraints.

Using tourmaline thermometry we have shown that the temperature at which the faults at Val-d'Or slipped at was approximately 308˚C. Tensile testing of tourmaline crystals growing parallel to the shear direction yields a proxy shear stress value of 44 MPa (Fig. 2.11), and we assume a total shear stress drop of 44 MPa based on previous descriptions of stress field

rotations (Fig. 3.1). For faults with 56˚, 60˚, and 70˚ dips the respective σ_D values are 105 MPa, 51 MPa and 35 MPa. σ_L was estimated from lithostatic pressure and geothermal gradients to give a range of 258-307 MPa. The pressure at which the low salinity hydrothermal fluid undergoes a phase separation P_E was calculated to be 9-10 MPa. This gives a maximum pressure drop of 222-267 MPa (Fig. 3.1). Considering our deformation temperature estimates, we conclude that fault-valve behavior in the structures at Val-d'Or was occurring as deep as ~10 km. Given these depths and our estimates of σ_D, we conclude that a high pore fluid factor (λ=0.9) would be necessary for failure.

3. 2 *Looking Forward*

A major limitation of this project was the quality of exposure in the field. At the Triangle mine all exposed structures were in stopes that were destroyed daily, and the mining schedule allowed for short visits of less than one hour at each stope. Multiple visits to the same stope was virtually impossible. It would have been a great benefit to this research to have been able to spend more time studying the structures exposed in the stopes. In addition, at the time of our fieldwork the Triangle mine had only reached approximately 300m depth, while drill cores had shown that the deposit extended to depths greater than 1000 m. It would be of great interest to investigate if and how the structural framework and mineral chemistry changes with increasing depth in the deposit. The Lamaque mine was an open pit with an inaccessible underground section. A chief issue with the structures at Lamaque were that many of them were either mined out or too large and poorly exposed to provide much information. Access to this underground section would have been very useful to provide further comparison to the Triangle mine.

Our tensile test results are truly only applicable to tourmalines at room temperature and pressure. Conducting tensile tests on tourmalines at higher temperatures would provide better constraints on the structures at the depths at which they were deforming. Ideally, such tests would be conducted at 300-400˚C as indicated by tourmaline intersector thermometry.

Higher temperature experiments (>600˚C) would be useful to determine at what temperature crystal plasticity is thermally activated in tourmaline.

Our calculated P_E does not take into account the CO_2 present in the fluid, which likely has a non-negligible effect on its magnitude. Robert and Kelly (1987) estimate that the hydrothermal fluid at Sigma contained 15-30 wt% CO_2, and our acid leeches show that hydrothermally altered rocks from Lamaque and Triangle contain 6-25 wt% CO_2. An improved calculation that considers the CO_2 content would improve the constrained ΔP value.

References

Anderson, E.M., 1905. The dynamics of faulting. Trans. Edinb. Geol. Soc. 8, 387–402. https://doi.org/10.1144/transed.8.3.387

Bedard, J.H., Harris, L.B., Thurston, P., 2013. The hunting of the snArc. Precambrian Res. 229, 20–48.

Boullier, A.-M., Robert, F., 1992. Palaeoseismic events recorded in Archaean gold-quartz vein networks, Val d'Or, Abitibi, Quebec, Canada. J. Struct. Geol. 14, 161–179. https://doi.org/10.1016/0191-8141(92)90054-Z

Bürgmann, R., Dresen, G., 2008. Rheology of the Lower Crust and Upper Mantle: Evidence from Rock Mechanics, Geodesy, and Field Observations. Annu. Rev. Earth Planet. Sci. 36, 531–567. https://doi.org/10.1146/annurev.earth.36.031207.124326

Büttner, S.H., Kasemann, S.A., 2007. Deformation-controlled cation diffusion in tourmaline: A microanalytical study on trace elements and boron isotopes. Am. Mineral. 92, 1862–1874. https://doi.org/10.2138/am.2007.2567

Byerlee, J., 1978. Friction of rocks. Pure Appl. Geophys. 116, 615–626. https://doi.org/10.1007/BF00876528

Cameron, E.M., Hattori, K., 1987. Archean gold mineralization and oxidized hydrothermal fluids. Econ. Geol. 82, 1177–1191. https://doi.org/10.2113/gsecongeo.82.5.1177

Couture, J.-F., Pilote, P., Machado, N., Desrochers, J.-P., 1994. Timing of gold mineralization in the Val-d'Or District, southern Abitibi Belt; evidence for two distinct mineralizing events. Econ. Geol. 89, 1542–1551. https://doi.org/10.2113/gsecongeo.89.7.1542

Cox, S.F., 2016. Injection-Driven Swarm Seismicity and Permeability Enhancement: Implications for the Dynamics of Hydrothermal Ore Systems in High Fluid-Flux, Overpressured Faulting Regimes—An Invited Paper. Bull. Soc. Econ. Geol. 111, 559–587.

Cox, S.F., Etheridge, M.A., Wall, V.J., 1987. The role of fluids in syntectonic mass transport, and the localization of metamorphic vein-type ore deposists. Ore Geol. Rev. 2, 65–86. https://doi.org/10.1016/0169-1368(87)90024-2

Daigneault, R., Perrault, G., Bedard, P., 1982. Geologie et geochimie de la mine Lamaque, Val d'Or, Quebec. Can. Min. Metall. Bull. 76, 111–127.

Dimroth, E., Imreh, L., Goulet, N., Rocheleau, M., 1983. Evolution of the south-central segment of the Archean Abitibi Belt, Quebec. Part II: Tectonic evolution and geomechanical model. Can. J. Earth Sci. 20, 1355–1373. https://doi.org/10.1139/e83-124

Döhmann, M.J.E.A., Brune, S., Nardini, L., Rybacki, E., Dresen, G., 2019. Strain Localization and Weakening Processes in Viscously Deforming Rocks: Numerical Modeling Based on Laboratory Torsion Experiments. J. Geophys. Res. Solid Earth 124, 1120–1137. https://doi.org/10.1029/2018JB016917

Dubé, J., 2018. Caractérisation métallogénique et structurale de la minéralisation aurifère des gisements Triangle et Cheminée No. 4, Val-d'Or, Abitibi, Québec.

Goldfarb, R.J., Groves, D.I., 2015. Orogenic gold: Common or evolving fluid and metal sources through time. Lithos 233, 2–26. https://doi.org/10.1016/j.lithos.2015.07.011

Goldfarb, R.J., Groves, D.I., Gardoll, S., 2001. Orogenic gold and geologic time: a global synthesis - ScienceDirect. Ore Geol. Rev. 18, 1–75. https://doi.org/10.1016/S0169-1368(01)00016-6

Griffith, A.A., 1921. The phenomena of rupture and flow in solids. Philos. Trans. R. Soc. Lond., Containing Papers of a Mathematical or Physical Character 221, 163–198. https://doi.org/10.1098/rsta.1921.0006

Groves, D.I., Goldfarb, R.J., Gebre-Mariam, M., Hagemann, S.G., Robert, F., 1998. Orogenic gold deposits: A proposed classification in the context of their crustal distribution and relationship to

other gold deposit types. Ore Geol. Rev. 13, 7–27. https://doi.org/10.1016/S0169-1368(97)00012-7
Hanes, J.A., Archibald, D.A., Hodgson, C.J., Robert, F., 1992. Dating of Archean auriferous quartz vein deposits in the Abitibi greenstone belt, Canada; 40 Ar/ 39 Ar evidence for a 70- to 100-m.y.-time gap between plutonism-metamorphism and mineralization. Econ. Geol. 87, 1849–1861. https://doi.org/10.2113/gsecongeo.87.7.1849
Hart, E.W., 1967. Theory of the tensile test. Acta Metall. 15, 351–355. https://doi.org/10.1016/0001-6160(67)90211-8
Henry, D.J., Dutrow, B.L., 1996. Metamorphic tourmaline and its petrologic applications. Rev. Mineral. Geochem. 33, 503–557.
Henry, D.J., Dutrow, B.L., 1992. Tourmaline in a low grade clastic metasedimentary rock: an example of the petrogenetic potential of tourmaline. Contrib. Mineral. Petrol. 112, 203–218. https://doi.org/10.1007/BF00310455
Hill, D.P., 1992. Temperatures at the Base of the Seismogenic Crust Beneath Long Valley Caldera, California, and the Phlegrean Fields Caldera, Italy, in: Gasparini, P., Scarpa, R., Aki, K. (Eds.), Volcanic Seismology, IAVCEI Proceedings in Volcanology. Springer Berlin Heidelberg, pp. 432–461.
Hinsberg, V.V., Schumacher, J.C., 2007. Intersector element partitioning in tourmaline: a potentially powerful single crystal thermometer. Contrib. Mineral. Petrol. 153 (3), 289–301. https://doi.org/10.1007/s00410-006-0147-7
Holmgren, M., 2006. X Steam, Thermodynamic properties of water and steam.
Hubert, C., Trudel, P., Gélinas, L., 1984. Archean wrench fault tectonics and structural evolution of the Blake River Group, Abitibi Belt, Quebec. Can. J. Earth Sci. 21, 1024–1032. https://doi.org/10.1139/e84-107
Jébrak, M., LeQuentrec, M.F., Mareschal, J.-C., Blais, D., 1991. A gravity survey across the Bourlamaque massif, southeastern Abitibi greenstone belt, Québec, Canada: the relationship between the geometry of tonalite plutons and associated gold mineralization. Precambrian Res. 50, 261–268. https://doi.org/10.1016/0301-9268(91)90024-5
Kerrich, R., 1986. Fluid infiltration into fault zones: Chemical, isotopic, and mechanical effects. Pure Appl. Geophys. 124, 225–268. https://doi.org/10.1007/BF00875727
Kerrich, R., Allison, I., 1978. Vein geometry and hydrostatics during Yellowknife mineralisation. Can. J. Earth Sci. 15, 1653–1660. https://doi.org/10.1139/e78-169
Kimura, N., Awaji, H., Okamoto, M., Matsumura, Y., Masuda, T., 2006. Fracture strength of tourmaline and epidote by three-point bending test: application to microboudin method for estimating absolute magnitude of palaeodifferential stress - ScienceDirect. J. Struct. Geol. 28, 1093–1102.
Kranz, R.L., 1980. The effects of confining pressure and stress difference on static fatigue of granite. J. Geophys. Res. Solid Earth 85, 1854–1866. https://doi.org/10.1029/JB085iB04p01854
Machado, N., Gariepy, C., Phillippe, S., David, J., 1991. Géochronologie U–Pb du territoire québécois: Fosses du Labrador et de l'Ungava et Sous-province de Pontiac. (No. MB 91-07). Ministére de l'Énergie et des Ressources, Quebec.
Micklethwaite, S., 2013. Fault stepovers and gold mineralisation, in: MINERAL DEPOSIT RESEARCH FOR A HIGH-TECH WORLD, 12th SGA Biennial Meeting 2013. Uppsala, Sweden.
Micklethwaite, S., Ford, A., Witt, W., Sheldon, H.A., 2014. The where and how of faults, fluids and permeability – insights from fault stepovers, scaling properties and gold mineralisation. Geofluids 15, 1–12.

Monecke, T., Mercier-Langevin, P., Dubé, B., Frieman, B.M., 2017. Geology of the Abitibi Greenstone Belt, in: Archean Base and Precious Metal Deposits, Southern Abitibi Greenstone Belt, Canada. Society of Economic Geologists. https://doi.org/10.5382/Rev.19.01

Neumayr, P., Hagemann, S.G., 2000. Structural setting, textures, and timing of hydrothermal vein systems in the Val d'Or camp, Abitibi, Canada: implications for the evolution of transcrustal, second- and third-order fault zones and gold mineralization 37, 20.

Neumayr, P., Hagemann, S.G., Banks, D.A., 2007. Fluid chemistry and evolution of hydrothermal fluids in an Archaean transcrustal fault zone network: The case of the Cadillac Tectonic Zone, Abitibi greenstone belt, Canada. Can. J. Earth Sci. 44, 745–773.

Passchier, C.W., Trouw, R.A.J., 2005. Microtectonics, 2nd ed. Springer-Verlag Berlin Heidelberg.

Perrault, G., Trudel, P., Bedard, P., 1984. Auriferous halos associated with the gold deposits at Lamaque Mine, Quebec. Econ. Geol. 79, 227–238. https://doi.org/10.2113/gsecongeo.79.2.227

Phillips, G.N., Powell, R., 2010. Formation of gold deposits: a metamorphic devolatilization model. J. Metamorph. Geol. 28, 689–718. https://doi.org/10.1111/j.1525-1314.2010.00887.x

Robert, F., Brown, A.C., 1986a. Archean gold-bearing quartz veins at the Sigma Mine, Abitibi greenstone belt, Quebec; Part II, Vein paragenesis and hydrothermal alteration. Econ. Geol. 81, 593–616. https://doi.org/10.2113/gsecongeo.81.3.593

Robert, F., Brown, A.C., 1986b. Archean gold-bearing quartz veins at the Sigma Mine, Abitibi greenstone belt, Quebec; Part I, Geologic relations and formation of the vein system. Econ. Geol. 81, 578–592. https://doi.org/10.2113/gsecongeo.81.3.578

Robert, F., Kelly, W.C., 1987. Ore-forming fluids in Archean gold-bearing quartz veins at the Sigma Mine, Abitibi greenstone belt, Quebec, Canada. Econ. Geol. 82, 1464–1482. https://doi.org/10.2113/gsecongeo.82.6.1464

Scholz, C.H., 1988. The brittle-plastic transition and depth of seismic faulting. Geol. Rundsch. 77, 319–328.

Secor, D.T.Jr., 1965. Role of pore pressure in jointing. Am. J. Sci. 263, 633–646.

Sherlock, R.L., Jowett, E.C., Smith, B.D., Irish, D.E., 1993. Distinguishing barren and auriferous veins in the Sigma Mine, Val-d'Or, Quebec. Can. J. Earth Sci. 30, 413–419. https://doi.org/10.1139/e93-030

Sibson, R., 2014. Earthquake Rupturing in Fluid-Overpressured Crust: How Common? Pure Appl. Geophys. 171, 2867–2885.

Sibson, R., 1990. Rupture Nucleation on Unfavorably Oriented Faults. Bull. Seismol. Soc. Am. 80, 1580–1604.

Sibson, R.H., 2007. An episode of fault-valve behaviour during compressional inversion? — The 2004 MJ6.8 Mid-Niigata Prefecture, Japan, earthquake sequence. Earth Planet. Sci. Lett. 257, 188–199. https://doi.org/10.1016/j.epsl.2007.02.031

Sibson, R.H., 1992. Implications of fault-valve behaviour for rupture nucleation and recurrence. Tectonophysics 211, 283–293.

Sibson, R.H., 1990. Conditions for fault-valve behaviour. Geol. Soc. Lond. Spec. Publ. 54, 15–28. https://doi.org/10.1144/GSL.SP.1990.054.01.02

Sibson, R.H., 1977. Fault rocks and fault mechanisms. J. Geol. Soc. 133, 191–213. https://doi.org/10.1144/gsjgs.133.3.0191

Sibson, R.H., Robert, F., Poulsen, K.H., 1988. High-angle reverse faults, fluid-pressure cycling, and mesothermal gold-quartz deposits. Geology 16, 551. https://doi.org/10.1130/0091-7613(1988)016<0551:HARFFP>2.3.CO;2

Stesky, R.M., 1978. Rock friction-effect of confining pressure, temperature, and pore pressure. Pure Appl. Geophys. 116, 15.

Völker, D., Grevemeyer, I., Stipp, M., Wang, K., He, J., 2011. Thermal control of the seismogenic zone of southern central Chile. J. Geophys. Res. Solid Earth 116. https://doi.org/10.1029/2011JB008247

Warren-Smith, E., Fry, B., Wallace, L., Chon, E., Henrys, S., Sheehan, A., Mochizuki, K., Schwartz, S., Webb, S., Lebedev, S., 2019. Episodic stress and fluid pressure cycling in subducting oceanic crust during slow slip. Nat. Geosci. 12, 475–481. https://doi.org/10.1038/s41561-019-0367-x

Williams, R.T., 2019. Coseismic boiling cannot seal faults: Implications for the seismic cycle. Geology 47, 461–464.

Wong, L., Davis, D.W., Krogh, T.E., Robert, F., 1991. UPb zircon and rutile chronology of Archean greenstone formation and gold mineralization in the Val d'Or region, Quebec. Earth Planet. Sci. Lett. 104, 325–336. https://doi.org/10.1016/0012-821X(91)90213-2

Appendices

sample	cation	sector	cpfu	sector	cpfu	D	T (C)	Medians
112B	Ca	c-	0.132607	a	0.043644	0.329124	313	
112B	Ca	c-	0.132607	a	0.04373	0.329771	314	
112B	Ca	c-	0.13	a	0.041845	0.352236	306	
112B	Ca	c-	0.128271	a	0.045182	0.314348	339	**313**
112B	Ca	c-	0.138412	a	0.043509	0.27614	295	
112B	Ca	c-	0.131963	a	0.03644	0.639009	242	
112B	Ca	c-	0.13529	a	0.086451	0.659593	426	
112B	Ca	c-	0.13	a	0.08	0.363636	428	
112B	Ca	c-	0.129291	a	0.036646	0.8	187	
102	Ca	c-	0.114108	a	0.03502	0.305302	350	
102	Ca	c-	0.154068	a	0.047037	0.376328	283	**298**
102	Ca	c-	0.148657	a	0.047079	0.307077	298	
6	Ca	c-	0.078988	a	0.029725	0.608987	361	**312**
6	Ca	c-	0.090864	a	0.027902	0.401811	285	
6	Ca	**c+**	0.040835	a	0.120012	1.312981	312	
4	Ca	**c+**	0.022742	a	0.083995	3.504578	174	**209**
S4	Ca	**c+**	0.022838	a	0.080253	3.513962	209	
S4	Ca	**c+**	0.024622	a	0.078301	3.180166	275	
S4	Ca	**c+**	0.023087	a	0.082177	3.559419	199	
S4	Ca	**c+**	0.022864	a	0.080127	3.504578	210	

Table 1. Tourmaline thermometry results.

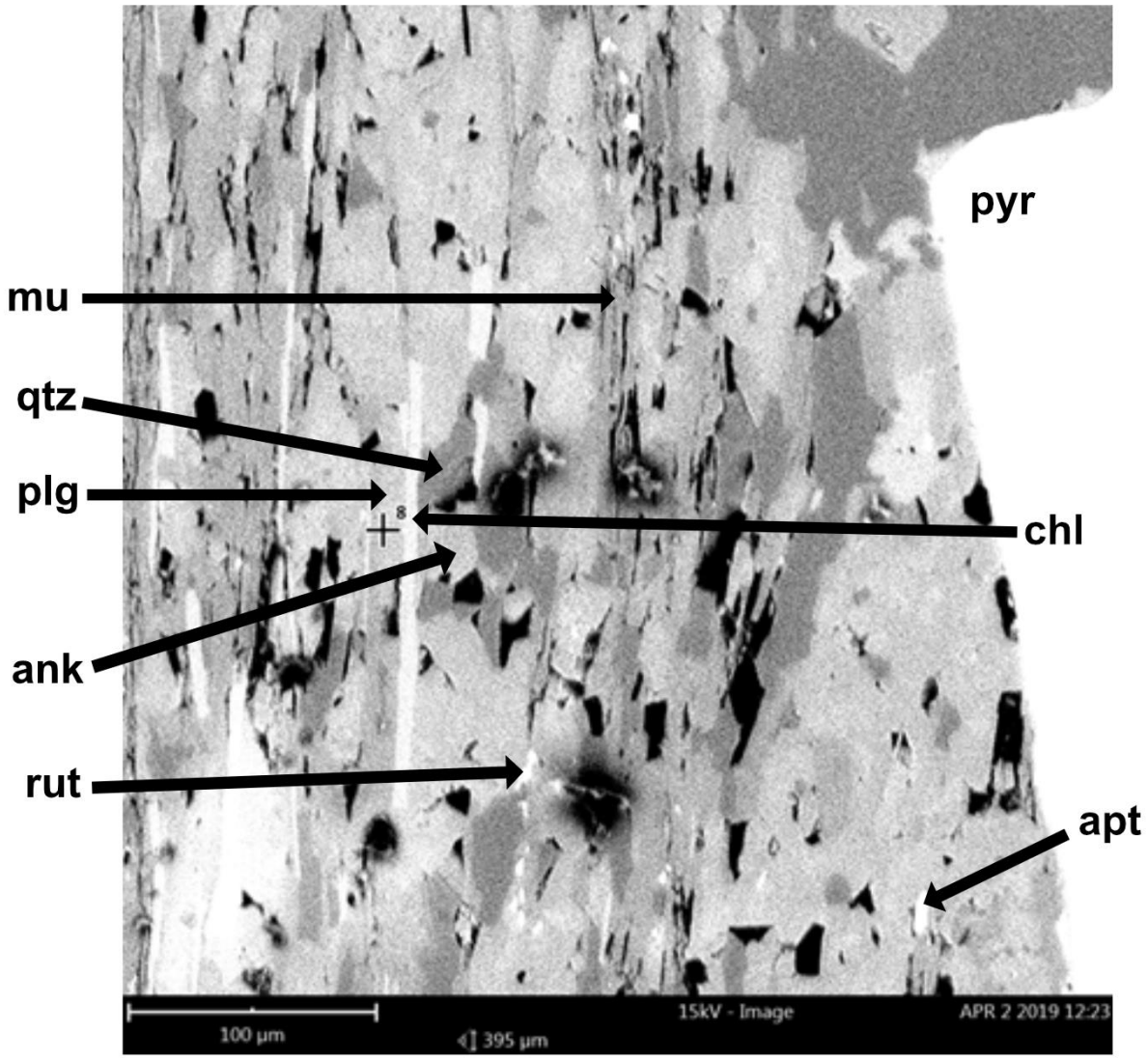

Figure A. BSE image of hydrothermally altered metavolcanic from Triangle. Sample NO18-37. Mineralogy includes chlorite (chl), muscovite (mu), ankerite (ank), quartz (qtz), plagioclase (plg), pyrite (pyr), rutile (rut), apatite (apt).